



105
253
THS

MICHIGAN STATE UNIVERSITY LIBRARIES



3 1293 00904 9408

This is to certify that the
thesis entitled
**Intermediate Mass Fragment Multiplicities in
Heavy-Ion Collisions**

presented by

Joy Ann Conrad

has been accepted towards fulfillment
of the requirements for

M.S. degree in Physics

Ray D. Wright
Major professor

Date August 5, 1993

**LIBRARY
Michigan State
University**

**PLACE IN RETURN BOX to remove this checkout from your record.
TO AVOID FINES return on or before date due.**

DATE DUE	DATE DUE	DATE DUE
_____	_____	_____
_____	_____	_____
_____	_____	_____
_____	_____	_____
_____	_____	_____
_____	_____	_____
_____	_____	_____

MSU Is An Affirmative Action/Equal Opportunity Institution

c:\circ\datedue.pm3-p.1

INTERMEDIATE MASS FRAGMENT
MULTIPLICITIES IN HEAVY-ION
COLLISIONS

By

Joy Ann Conrad

A THESIS

Submitted to
Michigan State University
in partial fulfillment of the requirements
for the Degree of

MASTER OF SCIENCE

Department of Physics and Astronomy

1993

ABSTRACT

INTERMEDIATE MASS FRAGMENT MULTIPLICITIES IN HEAVY-ION COLLISIONS

By

Joy Ann Conrad

The average multiplicities of intermediate mass fragments (IMF's) for the most central of nucleus-nucleus collisions in the (nearly) symmetric systems: $^{20}\text{Ne}+^{27}\text{Al}$, $^{40}\text{Ar}+^{45}\text{Sc}$, $^{84}\text{Kr}+^{93}\text{Nb}$, and $^{129}\text{Xe}+^{139}\text{La}$, each at a wide range of intermediate beam energies, are studied. Cuts allowing the top 10% of the spectra of observables assumed to be correlated with the impact parameter are utilized to select small impact parameters. An investigation is conducted to determine the extent to which the measurements of the average multiplicities of IMF's are biased by an auto-correlation between the number of IMF's and the centrality condition. The two observables least auto-correlated with the number of intermediate mass fragments are identified, then used to select the most central events. The system mass and beam energy dependence of IMF multiplicities measured in a nearly 4π detector is then presented.

ACKNOWLEDGEMENTS

I thank Bill Llope for all of his patience in helping me with this analysis; Gary Westfall, my advisor, for coordinating the whole project; and the entire 4π group for collecting the data: Darren Craig, Gene Gualtieri, Stephan Hannuschke, Tong Li, Robert Pak, Nathan Stone, Skip Vander Molen, Jaeyong Yee, and Sherry Yennello.

Contents

LIST OF TABLES	v
LIST OF FIGURES	vi
1 Introduction	1
2 Experimental Details	5
3 Selection of Central Collisions	7
3.1 Centrality Variables	7
3.2 Auto-Correlations	29
4 Most Central Collisions	35
5 Discussion	43
6 Summary and Conclusions	47
LIST OF REFERENCES	49

List of Tables

3.1	The most efficient centrality variables for these data taken from the event shape analysis of Reference [1].	9
-----	--	---

List of Figures

3.1	The entrance channel mass dependance of the average multiplicity of intermediate mass fragments versus the number of charged particles for specified beam energies	12
3.2	The entrance channel mass dependance of the average multiplicity of intermediate mass fragments versus the charge detected at mid-rapidity for specified beam energies	13
3.3	The entrance channel mass dependance of the average multiplicity of intermediate mass fragments versus the total transverse kinetic energy for specified beam energies	14
3.4	The system mass dependance of the emission of intermediate mass fragments as a function of the total transverse kinetic energy of the particles	16
3.5	The entrance channel mass dependance of the average multiplicity of intermediate mass fragments versus the number of hydrogen isotopes for specified beam energies	18
3.6	The entrance channel mass dependance of the average multiplicity of intermediate mass fragments versus the charge of the hydrogen and helium isotopes for specified beam energies	19
3.7	The beam energy dependance of the average multiplicity of intermediate mass fragments versus the number of charged particles for each of the four systems	21
3.8	The beam energy dependance of the average multiplicity of intermediate mass fragments versus the charge detected at mid-rapidity for each of the four systems	22
3.9	The beam energy dependance of the average multiplicity of intermediate mass fragments versus the total transverse kinetic energy for each of the four systems	23
3.10	The beam energy dependance of the average multiplicity of intermediate mass fragments versus the number of hydrogen isotopes for each of the four systems	24
3.11	The beam energy dependance of the average multiplicity of intermediate mass fragments versus the charge of the hydrogen and helium isotopes for each of the four systems	25

3.12	The beam energy dependance of the means and the widths of the intermediate mass fragment multiplicity distributions for the events selected by 10% cuts on each of the five centrality variables separately	27
3.13	The average values, widths, and reduced widths of the multiplicities of intermediate mass fragments in the events selected by ~10% cuts on the largest values of six centrality variables versus the beam energies for $^{20}\text{Ne}+^{27}\text{Al}$ and $^{40}\text{Ar}+^{45}\text{Sc}$ entrance channels	31
3.14	The average values, widths, and reduced widths of the multiplicities of intermediate mass fragments in the events selected by ~10% cuts on the largest values of six centrality variables versus the beam energies for $^{84}\text{Kr}+^{93}\text{Nb}$ and $^{129}\text{Xe}+^{139}\text{La}$ entrance channels	32
4.1	The mean number of intermediate mass fragments versus the beam energy for the events selected by the two most efficient centrality variables according to Reference [1]	37
4.2	The mean number of intermediate mass fragments versus the beam energy for the events selected using the two centrality variables that were seen to be free from auto-correlations with the number of intermediate mass fragments and of relatively high efficiency according to Reference [1]	39
4.3	The mean number of intermediate mass fragments as a function of projectile energy for all of the systems	41
5.1	A qualitative comparison of the average number of intermediate mass fragments versus the entrance channel mass in symmetric (this work) versus asymmetric (Reference [3]) entrance channels	45

Chapter 1

Introduction

To better understand the processes involved in nuclear collisions, experiments are performed which collide a projectile nucleus and a stationary target nucleus and utilize electronic devices to measure the particles and fragments that are emitted. An analysis is then conducted using the detected particle information to understand the mechanisms governing nucleus-nucleus collisions. There are many general theories that may describe the nature of the processes controlling the emission of detected particles. These models differ, however, in terms of the predicted number of intermediate mass fragments, i.e. particles with $3 \leq Z \lesssim 20$ [6] [10,11].

In one such description, the first stage of the reaction is a compression of the projectile-target system followed by an expansion to low densities. Density fluctuations are then responsible for the formation of detectable intermediate mass fragments [13-15]. Another possibility is that the collision compresses and expands leaving an excited nuclear residue that decays via the emission of particles [16,17]. This decay of such a residue may occur in one of two general ways: “sequentially” through the emission of predominately light charged particles [21] such as hydrogens or heliums over long time scales, or “simultaneously” through the emission of relatively large numbers of intermediate mass fragments [22] (IMF’s for which $3 \leq$

$Z \lesssim 20$) over much shorter time scales.

Sequential decays have been observed in excited nuclear systems with relatively low total excitation energies. These relatively slower decays (~ 1000 fm/c) [18] are generally understood to behave statistically with well defined transition rates based on the conservation of energy and angular momentum. Such excited systems periodically emit particles that reduce the excitation energy of the system by discrete amounts. These amounts are determined by the internal energy needed for the decay and the kinetic energy of the exiting particles. The mass and kinetic energy of the particles emitted are determined by the available excitation energy of the system as well as the height of the Coulomb and angular momentum barriers over which the particles must pass in order to escape. In this type of decay, large fragments may be emitted only in the first stages of the decay; however, due to generally lower barriers overall, light particle emission is always favored.

Sequential decays are reminiscent of the cooling of liquids by evaporation. This type of decay should not be confused with the complete vaporization of the systems that occurs at beam energies on the order of hundreds of MeV/nucleon. This “gaseous” phase is also characterized by the experimental detection of large numbers of predominately light charged particles.

At higher excitation energies than those exhibiting sequential decays, multifragmentation becomes an important process characteristic of the “liquid-gas” phase transition region. These decays are more rapid (~ 100 fm/c) [19,20] than sequential decays and result in the emission of relatively many more IMF’s. There have been many theories attempting to describe the processes governing multifragment emission, and these models have met varying degrees of success.

The number of intermediate mass fragments (N_{imf}) emitted in a nucleus-nucleus

collision is thus expected to be sensitive to the characteristics of the mechanisms governing the evolution of the excited nuclei formed in heavy-ion collisions. Since the transition from the liquid phase to the gaseous phase is expected to correspond to maximal numbers of IMF's [3] [8], IMF multiplicity distributions can be used to locate such transition regions if they occur.

It is the purpose of this work to accurately measure the average number of intermediate mass fragments ($\langle N_{imf} \rangle$) detected in central nucleus-nucleus collisions. A wide range of beam energies and entrance channel masses are available for this study. From this, it is hoped that particular regions dominated by sequential or multifragmentation decays will be identified, as well as possible transition regions between the two.

The most central collisions of the projectile and target nuclei result in the most violent collisions and lead to the largest possible excitation energies and systems for a given entrance channel and beam energy. The excitation energies in these collisions should also be more equilibrated, as compared to peripheral collisions, due to the larger number of nucleon-nucleon collisions. The most central collisions also result in systems with low angular momentum and hence approach conditions for which the center of momentum frame is the rest frame of the excited nuclear system.

Information concerning the impact parameter is then needed to select these most central collisions. Unfortunately, the impact parameter cannot be directly measured in a nuclear collision - it must be inferred from the experimental observables. Six such observables will be assumed to be correlated with the impact parameter, and cuts of each of these will be used to select the most central collisions.

Precaution will be taken to assure that the observables used to determine the impact parameter are not otherwise related to the multiplicity of IMF's. Any "auto-

correlation” between the observables used to select central collisions and the multiplicity of the IMF’s is a source of bias. Great care will be taken in this study to locate the observables correlated with the impact parameter that are not also auto-correlated with the mean number of intermediate mass fragments.

This thesis is organized as follows: Chapter 2 will contain experimental details in which the specifics of the detector, targets, and projectiles will be discussed. Chapter 3 will determine the most appropriate centrality variables for this analysis. Chapter 4 will display the results of the thesis - the mean number of IMF’s as a function of projectile energy and entrance mass for the most central collisions. Chapter 5 will compare these results to previous work, and Chapter 6 will provide a summary, as well as draw some conclusions based on this analysis.

Chapter 2

Experimental Details

The experimental data from nucleus-nucleus collisions was collected with the Michigan State University 4π array [2] at the National Superconducting Cyclotron Laboratory (NSCL) using beams extracted from the K1200 cyclotron. Four systems are analyzed over a wide range of beam energies. The (nearly) symmetric systems studied are: $^{20}\text{Ne}+^{27}\text{Al}$ at 55, 75, 95, 105, 115, 125, 135 MeV/nucleon; $^{40}\text{Ar}+^{45}\text{Sc}$ at 15, 25, 35, 45, 65, 75, 85, 95, 105, 115 MeV/nucleon; $^{84}\text{Kr}+^{93}\text{Nb}$ at 35, 45, 55, 65, 75 MeV/nucleon; and $^{129}\text{Xe}+^{139}\text{La}$ at 25, 35, 45, 50, 55, 60 MeV/nucleon.

The targets consisted of 1 mg/cm² of natural aluminum, 1.6 mg/cm² of natural scandium, 1 mg/cm² of natural niobium, and 1 mg/cm² of natural lanthanum. The projectile beam intensities were approximately 100 electrical pA [7].

The outer layer of the main 4π ball consists of 170 fast/slow plastic scintillator telescopes known as “phoswich” detectors and a forward array of 45 phoswich telescopes. The detectors in the main ball are arranged in 20 hexagonal and 10 pentagonal subarrays. In front of the main phoswich detectors are an additional 30 Bragg curve counters. The five forward most Bragg curve counters are subdivided into six subelements each for a total of 55 separate BCC’s. These Bragg curve detectors use an ionizing chamber of either P5 (95% argon, 5% methane) or C₂F₆ gas

at pressures of 500 and 100 torr, respectively.

The scintillators use the well known phoswich gating technique to determine the kinetic energy and charge information of particles that pass through the fast plastic and stop in the slow plastic. The BCC's provide similar E and ΔE information for those particles that pass through the BCC's and stop in the fast plastic. The overall kinetic energy thresholds are ~ 20 MeV for protons, ~ 3 MeV/nucleon for $Z=3$ fragments, and ~ 5 MeV/nucleon for $Z=12$ fragments. The 4π array is capable of efficiently detecting particles of charges ranging from $Z=1$ to $Z \lesssim 20$.

An event was defined as collisions resulting in at least two hits registered by any two phoswich detectors. Hits with Z values that fell "between bands" in the calibration of the electronic signals or that stopped in the fast plastic but contained no BCC information were rejected.

The overall geometrical acceptance of the detector is approximately 85% of 4π . The acceptance in the main part of the ball consisting of the scintillators and Bragg curve counters is greater than $\sim 90\%$. This region covers laboratory angles of $\sim 18^\circ$ to $\sim 160^\circ$. The forward array covers polar angles from $\sim 6^\circ$ to $\sim 18^\circ$ and has a geometrical acceptance of $\sim 50\%$. Due to the relatively poor acceptance for forward angles, the most central collisions will be selected for this analysis. For these, the experimental results are less significantly compromised by the geometrical inefficiencies of the apparatus.

Chapter 3

Selection of Central Collisions

3.1 Centrality Variables

In order to determine the impact parameter and hence select central collisions, the assumption was made that particular experimental observables are correlated with the impact parameter [1] [4]. The following six experimental observables can be used to select the most central collisions in this data:

(i) the number of charged particles (N_{chgd}) detected in each event.

(ii) the total charge of the detected particles in a software gate about “mid-rapidity” (Z_{MR}). This is thus defined to be the sum charge of all particles in the events for which:

$$.75y_T \leq y_{part} \leq .75y_P,$$

where the rapidity, y_{part} , of the particle is given by:

$$y_{part} = \frac{1}{2} \ln \frac{E_{part} + P_{part} \cos \theta}{E_{part} - P_{part} \cos \theta} - y.$$

In this equation, E_{part} represents the total energy, P_{part} the total momentum, and θ the polar angle of the particles in the center of momentum

frame. The rapidity of the center of momentum (y) with respect to the laboratory frame is given by:

$$y = \frac{1}{2} \ln \frac{1+b}{1-b}, \quad b = \frac{P_P}{E_P + M_T},$$

in which M_T represents the mass of the target (in MeV).

(iii) the transverse kinetic energy (KE_T) of the particles in the events.

This variable is defined as:

$$KE_T = \sum \frac{KE_{part}}{KE_P} \sin^2 \theta * 100,$$

where θ is the polar angle of the particle with respect to the beam axis, KE_{part} is the kinetic energy of each particle, and KE_P is the projectile kinetic energy in the laboratory. The factor of 100 is used for convenience.

(iv) the total number of hydrogen isotopes detected (N_H), which is the sum of all of the protons (A=1), deuterons (A=2), and tritons (A=3) detected.

(v) the total charge of all of the fragments registered in the detector (Z_{det}) in one event.

(vi) the total charge measured for hydrogen and helium isotopes (Z_{LCP}), which is the sum of the charge of all light charged particles detected in an event.

A previous study conducted by Llope *et al.* [1] determined which of these centrality variables was the most efficient in selecting central collisions in these data. This study has linked the emission patterns or “shapes” of the emitted particles with the impact parameter through an observable called the sphericity. The analysis was based on the assumption that central collisions would result in the most isotropic or spherical emission patterns of the events in the center of momentum frame.

The conclusion was drawn in Reference [1] that the variables that most efficiently allow the selection of the most central collisions vary with both the entrance channel mass of the system and the incident energy of the projectile. The best two variables for the selection of the smallest impact parameters from Reference [1] are shown in Table 3.1 for the systems and energies used herein. It should be noted that auto-correlations between these centrality variables and the event shapes were shown to be negligible if “moderate” centrality cuts were used (see Section 3.2). This does not mean that these variables are not auto-correlated with the observable used in this study, i.e. the number of intermediate mass fragments.

Table 3.1: The most efficient centrality variables for these data taken from the event shape analysis of Reference [1].

system	Projectile Energy (MeV/nucleon)				
	15	25	35	45	55 \Rightarrow
$^{20}\text{Ne}+^{27}\text{Al}$ ($A_{sys}=47$)					KE_T N_H
$^{40}\text{Ar}+^{45}\text{Sc}$ ($A_{sys}=85$)	N_H Z_{LCP}		N_H KE_T	KE_T N_H	
$^{84}\text{Kr}+^{93}\text{Nb}$ ($A_{sys}=177$)			Z_{MR} N_H	KE_T Z_{MR}	
$^{129}\text{Xe}+^{139}\text{La}$ ($A_{sys}=268$)		N_H Z_{LCP}	Z_{MR} Z_{LCP}	Z_{MR} KE_T	

As mentioned above, the number of IMF's detected in a heavy-ion collision is expected to be dependant on the mechanisms governing the nucleus-nucleus collisions. In order to study the most extreme conditions in nuclear matter, the most central collisions are of interest.

The mean number of IMF's is plotted versus values of each of the centrality variables in Figures 3.1- 3.11. These mean values are plotted for four overlapping projectile kinetic energy regions for each of the centrality variables. Figures 3.1- 3.6 show the variations in the mean number of IMF's as a function of entrance channel mass. In these Figures $^{20}\text{Ne}+^{27}\text{Al}$ is represented by asterisks, $^{40}\text{Ar}+^{45}\text{Sc}$ by circles, $^{84}\text{Kr}+^{93}\text{Nb}$ by triangles, and $^{129}\text{Xe}+^{139}\text{La}$ by stars. The error bars are statistical only, and these results have not been corrected for the experimental inefficiencies.

Figure 3.1 represents the experimental dependance of $\langle N_{imf} \rangle$ on the charged particle multiplicity, N_{chgd} , for four beam energies: 35 MeV/nucleon (upper left), 45 MeV/nucleon (upper right), 55 MeV/nucleon (lower left), and 75 MeV/nucleon (lower right). In these frames, there is a significant difference of IMF multiplicities for the various entrance channels of the same beam energy. The heaviest systems display the largest values of $\langle N_{imf} \rangle$, and the lighter systems display the smallest. The values of $\langle N_{imf} \rangle$ in the lighter systems, Ne+Al and Ar+Sc, display maximum average values near ~ 2 , while the heavier systems, Kr+Nb and Xe+La, show much larger numbers of IMF's, on average. The largest mean number of IMF's occurs for Xe+La collisions at the largest available beam energy (~ 55 MeV/nucleon).

These frames show that the average numbers of IMF's detected depends on the projectile - target combination and the beam energy. The heaviest systems emit the largest numbers of IMF's while the lightest systems emit the fewest.

In most cases in Figure 3.1, no maxima are statistically significant for a particular value of a centrality variable. Such maxima would indicate that an intermediate impact parameter would lead to maximal emissions of IMF's rather than a central collision. It was decided that the possible maxima in the Xe+La system at 55 MeV/nucleon and the Kr+Nb system at 75 MeV/nucleon were not statistically significant in these data.

Figure 3.2 represents the experimental values of $\langle N_{imf} \rangle$ versus the total detected charge at mid-rapidity, Z_{MR} . This plot is quantitatively different from the $\langle N_{imf} \rangle$ versus N_{chgd} plot of Figure 3.1 in that there is no significant variation of the mean number of IMF's with the entrance channel mass. This is notable considering that the entrance channel masses for the four systems range from 47 to 268 nucleons. The large number of IMF's from Z_{MR} cuts and the invariance with respect to the entrance mass could be the result of auto-correlations between Z_{MR} and $\langle N_{imf} \rangle$.

Figure 3.3 presents the experimental values of $\langle N_{imf} \rangle$ versus the total transverse kinetic energy, KE_T , of the events. Overall, the KE_T dependence illustrates a larger variation of the mean number of IMF's detected versus the system mass at specific beam energies than that observed versus the N_{chgd} or Z_{MR} variables in Figures 3.1 and 3.2.

The slopes of the mean number of IMF's as a function of KE_T in Figure 3.3 are observed to increase in apparently discrete increments for increasing entrance channel mass. Further investigation into this effect is illustrated in Figure 3.4. The top two plots in this Figure present the system mass dependence of the slopes, and the bottom four plots present the system mass dependence on $\langle N_{imf} \rangle$ for specified values of KE_T .

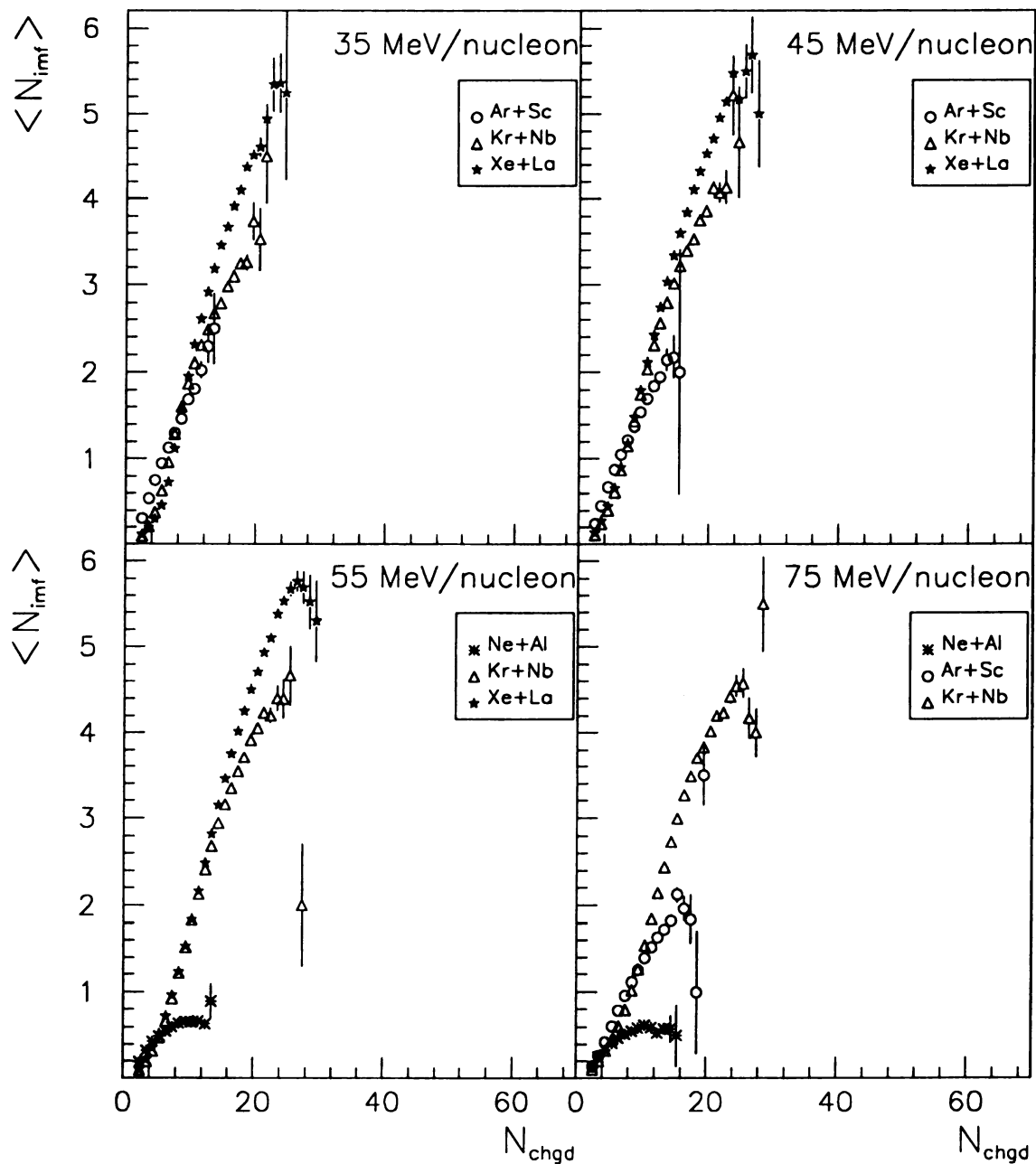


Figure 3.1: The entrance channel mass dependance of the average multiplicity of intermediate mass fragments versus the number of charged particles for specified beam energies is plotted above. The symbols represent the systems available for the beam energies: 35 MeV/nucleon (upper left), 45 MeV/nucleon (upper right), 55 MeV/nucleon (lower left), and 75 MeV/nucleon (lower right). Corrections due to auto-correlations and experimental acceptance have not yet been made.

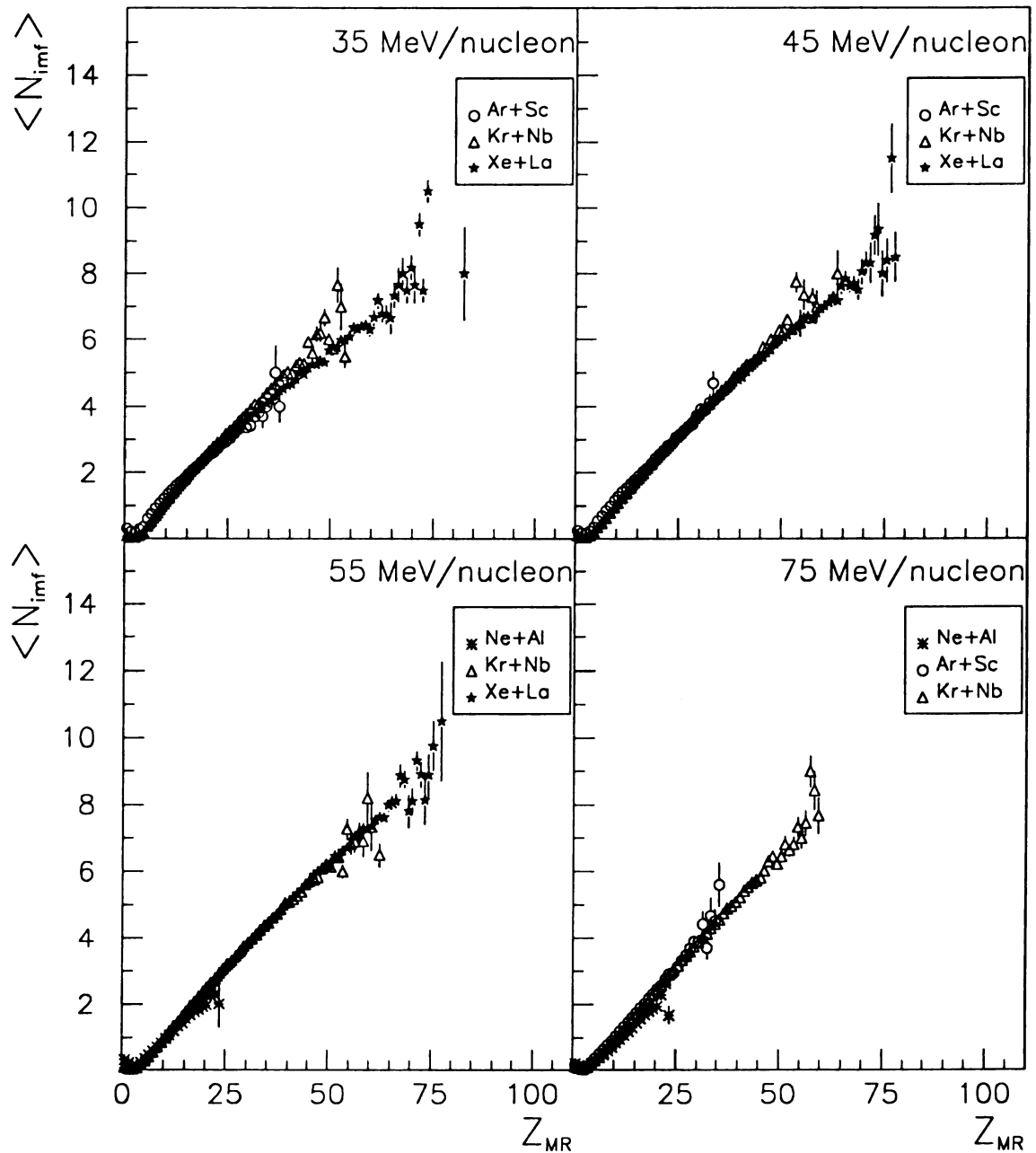


Figure 3.2: The entrance channel mass dependance of the average multiplicity of intermediate mass fragments versus the charge detected at mid-rapidity for specified beam energies is plotted above. The symbols represent the systems: $^{20}\text{Ne}+^{27}\text{Al}$ (asterisks), $^{40}\text{Ar}+^{45}\text{Sc}$ (circles), $^{84}\text{Kr}+^{93}\text{Nb}$ (triangles), and $^{129}\text{Xe}+^{139}\text{La}$ (stars), for the beam energies indicated above. The data above has not been corrected for auto-correlations between the observables or for the experimental inefficiencies of the detector.

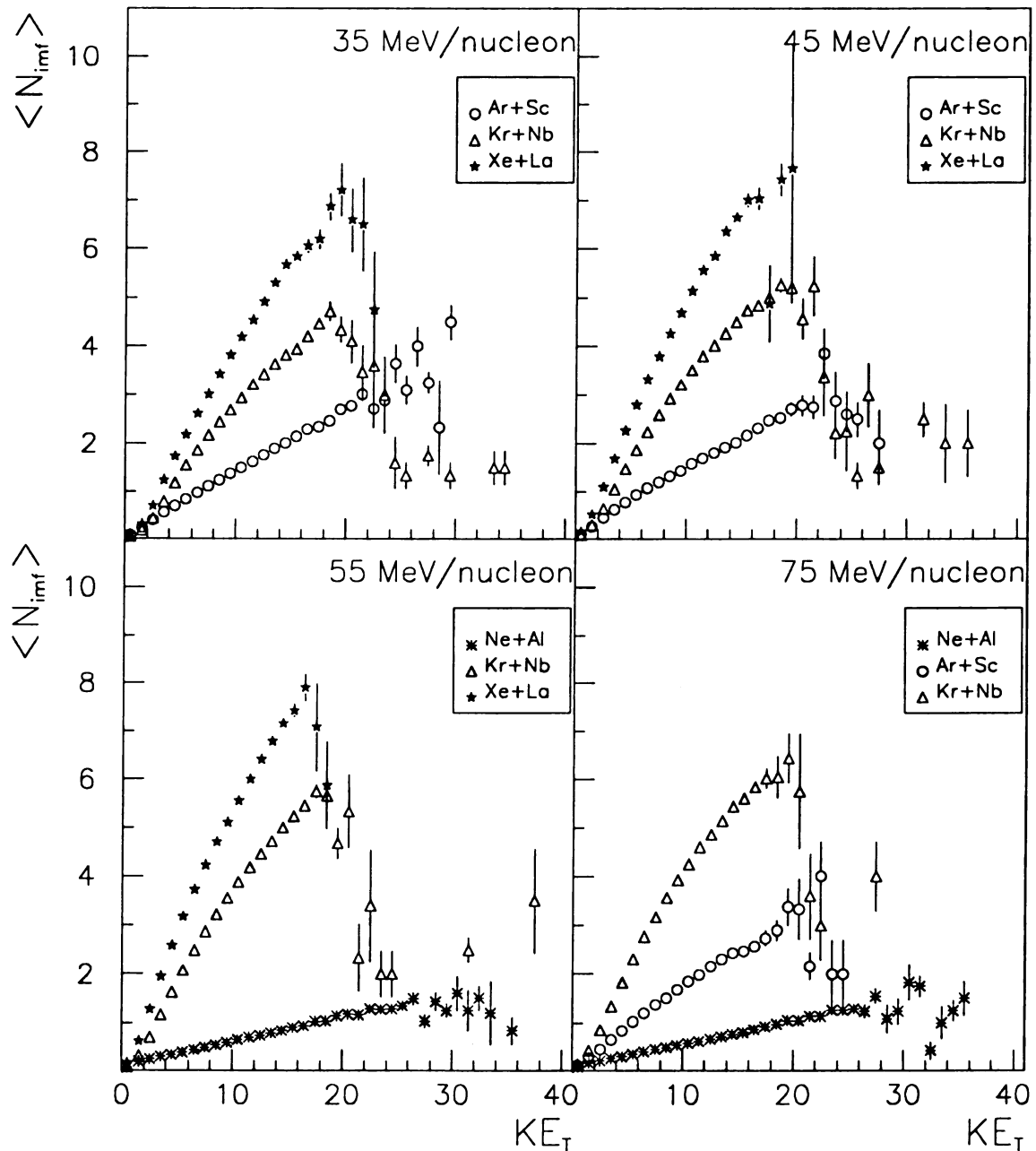


Figure 3.3: The entrance channel mass dependence of the average multiplicity of intermediate mass fragments versus the total transverse kinetic energy for specified beam energies is plotted above. The symbols represent the systems available for the beam energies: 35 MeV/nucleon (upper left), 45 MeV/nucleon (upper right), 55 MeV/nucleon (lower left), and 75 MeV/nucleon (lower right). Corrections due to auto-correlations and experimental acceptance have not yet been made.

The top left plot is the slopes of $\langle N_{imf} \rangle$ versus KE_T lines from Figure 3.3 as a function of incident projectile energy for the four systems. The Ne+Al system is represented by asterisks, the Ar+Sc system by circles, the Kr+Nb system by triangles, and the Xe+La system by stars. As illustrated in this plot, the heavier two systems, Kr+Nb and Xe+La, exhibit the largest variation in the slopes of the mean values.

The top right plot is the slope of $\langle N_{imf} \rangle$ versus KE_T plotted as a function of the charge (or mass) of the four systems. The three beam energies depicted in this plot are: 35 MeV/nucleon (squares), 45 MeV/nucleon (diamonds), and 55 MeV/nucleon (open crosses). This plot indicates that there is a general linear relationship between the $d\langle N_{imf} \rangle / dKE_T$ and the charge of the system for a 35 MeV/nucleon beam energy. This linear relationship breaks down, however, for higher projectile kinetic energies, perhaps due to the uncorrected experimental inefficiencies.

The bottom four plots in Figure 3.4 represent the relationship between the mean number of IMF's and the total entrance channel for several specified values of the total transverse kinetic energy. Four beam energies are plotted separately as indicated. Three different KE_T values were chosen: 8 (solid circles), 12 (solid squares), and 16 (solid triangles). As illustrated by the four bottom plots, for one value of the total transverse kinetic energy per event there is a linear relationship between average number of IMF's and the entrance channel charge.

In similarity to Figures 3.1, 3.2, and 3.3, the experimental values of $\langle N_{imf} \rangle$ versus the number of hydrogen fragments, N_H , and the total charge of the hydrogen and helium fragments, Z_{LCP} , are plotted in Figures 3.5 and 3.6, respectively. These Figures display large differences in the mean number of IMF's detected at different

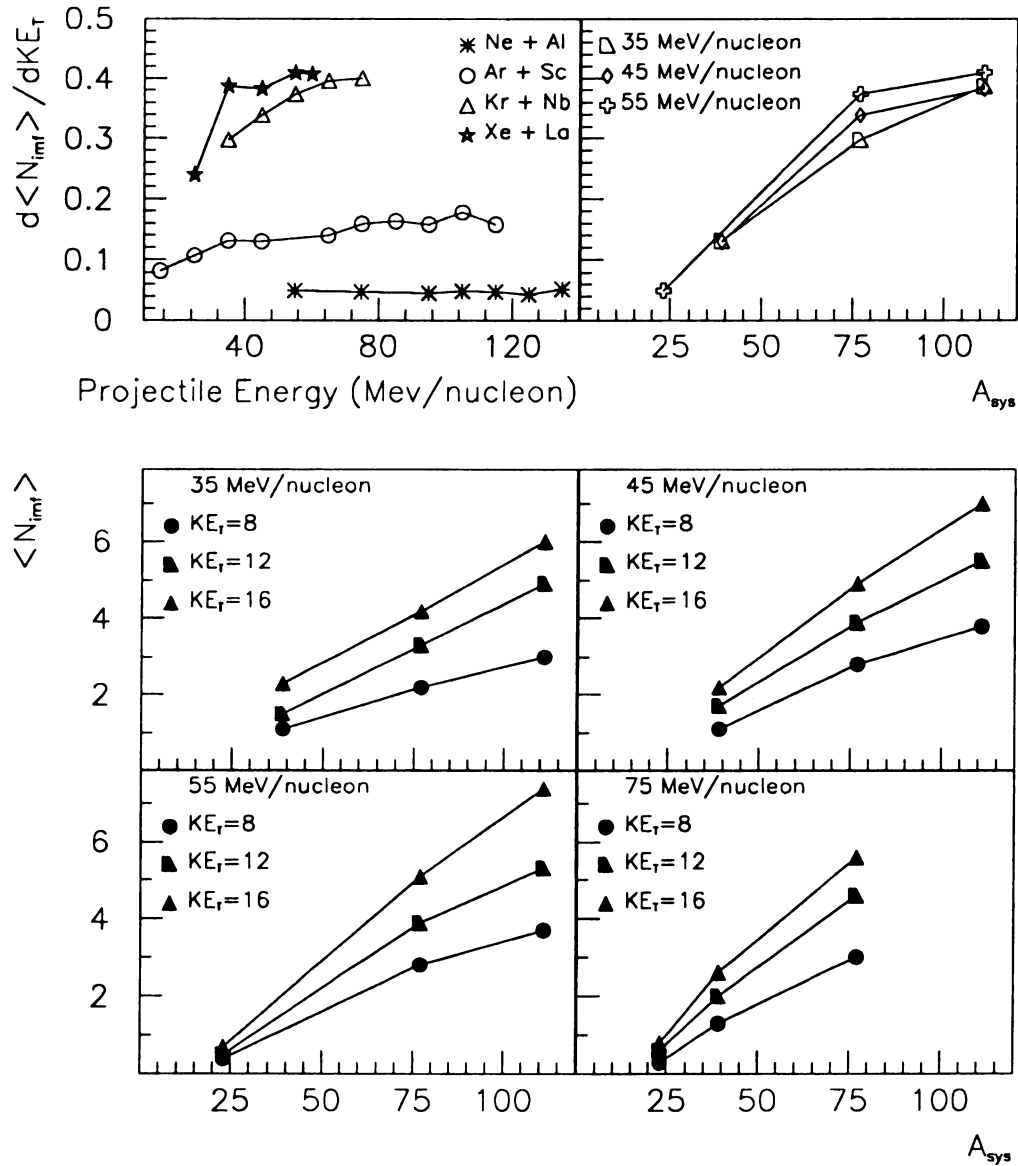


Figure 3.4: The system mass dependence of the emission of intermediate mass fragments as a function of the total transverse kinetic energy of the particles is plotted above. The top two plots are the slopes of the mean number of intermediate mass fragments versus the total transverse kinetic energy of the particles per event. The top left plot is the slopes as a function of beam energy, and the top right plot is the slopes as a function of the charge of the system. The bottom four plots are the mean number of intermediate mass fragments for one total particle kinetic energy value as a function of the charge of the system.

beam energies. These plots are also unique in the fact that plateau regions are observed which are not seen for the N_{chgd} , Z_{MR} , or KE_T dependence of $\langle N_{imf} \rangle$ shown previously. The variables N_H and Z_{LCP} are closely related by definition, and they each indicate that there is either a N_H or Z_{LCP} threshold where the number of IMF's emitted remains constant (a plateau region) or a threshold where the additional production of light particles results in a decrease in $\langle N_{imf} \rangle$ (a maximum). Also, these plots display the lowest average number of IMF's generated as compared to the curves shown in Figures 3.1- 3.3 of the other centrality variables.

It should be noted that $\langle N_{imf} \rangle$ from events with small N_H or Z_{LCP} values in Figures 3.5 and 3.6 are considered to correspond to events with large impact parameters. These values are then the result of experimental inefficiencies that are the most important in peripheral collisions.

The experimental $\langle N_{imf} \rangle$ values are also plotted versus the values of the various centrality variables in Figures 3.7- 3.11 for each system separately at specified beam energies. The symbols each represent one beam energy: 15 MeV/nucleon, solid triangles; 25 MeV/nucleon, diamonds; 35 MeV/nucleon, circles; 45 MeV/nucleon, open crosses; 55 MeV/nucleon, squares; 75 MeV/nucleon, open triangles; 115 MeV/nucleon, stars; and 135 MeV/nucleon, asterisks. The error bars depict the statistical errors of the mean values.

The plots of $\langle N_{imf} \rangle$ versus N_{chgd} in Figure 3.7 illustrate a significant beam energy dependence in the lighter two systems, Ne+Al and Ar+Sc, but a lesser beam energy dependence for the two heavier systems, Kr+Nb and Xe+La. This effect is in part due to a visual illusion caused by the smaller range of beam energies covered by the larger systems. The Ne+Al system results in the smallest numbers of IMF's of the four systems. The number of IMF's for this system was seen to decrease for

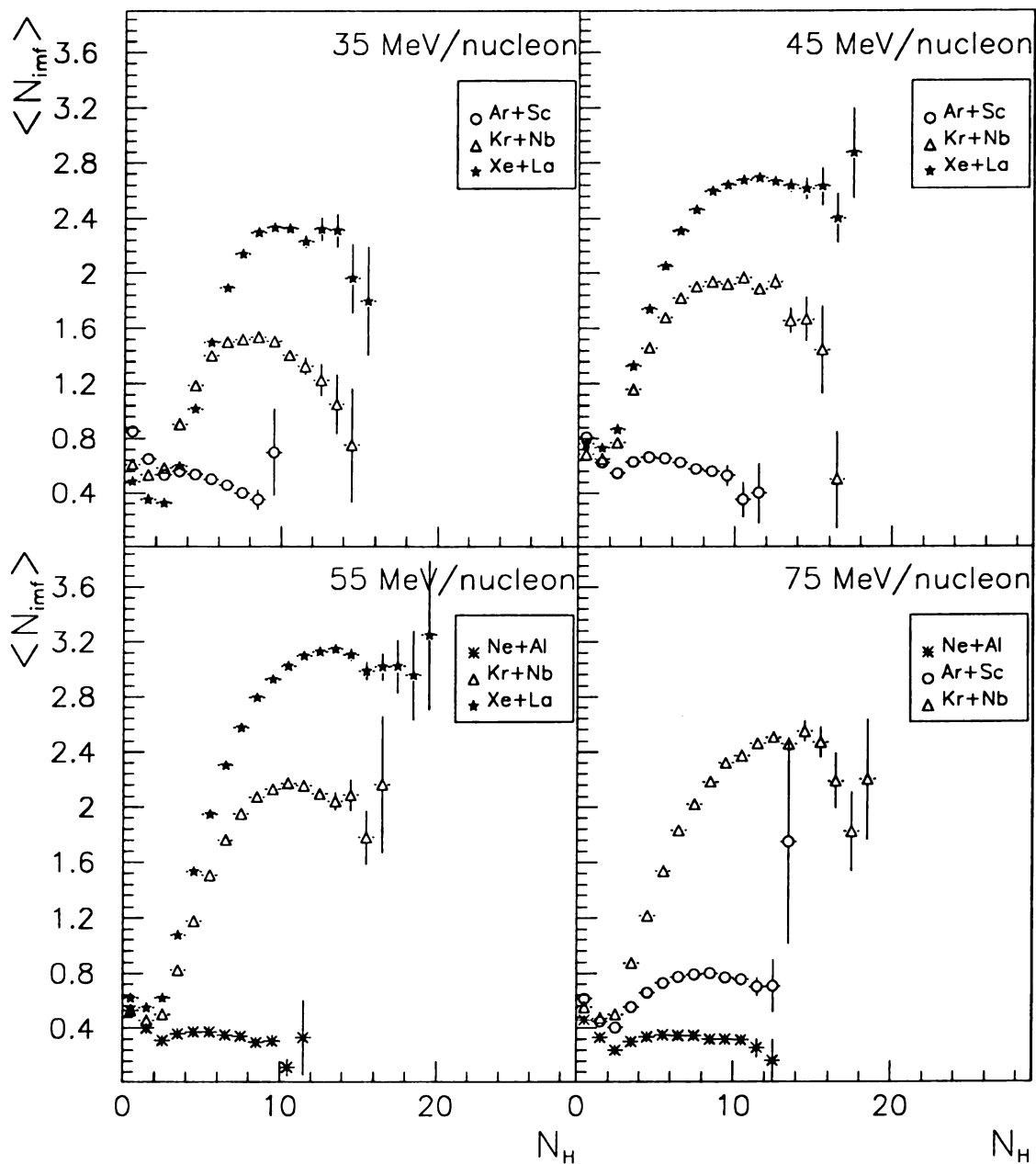


Figure 3.5: The entrance channel mass dependence of the average multiplicity of intermediate mass fragments versus the number of hydrogen isotopes for specified beam energies is plotted above. The symbols represent the systems: $^{20}\text{Ne}+^{27}\text{Al}$ (asterisks), $^{40}\text{Ar}+^{45}\text{Sc}$ (circles), $^{84}\text{Kr}+^{93}\text{Nb}$ (triangles), and $^{129}\text{Xe}+^{139}\text{La}$ (stars), for the beam energies indicated above. The data above has not been corrected for auto-correlations between the observables or for the experimental inefficiencies of the detector.

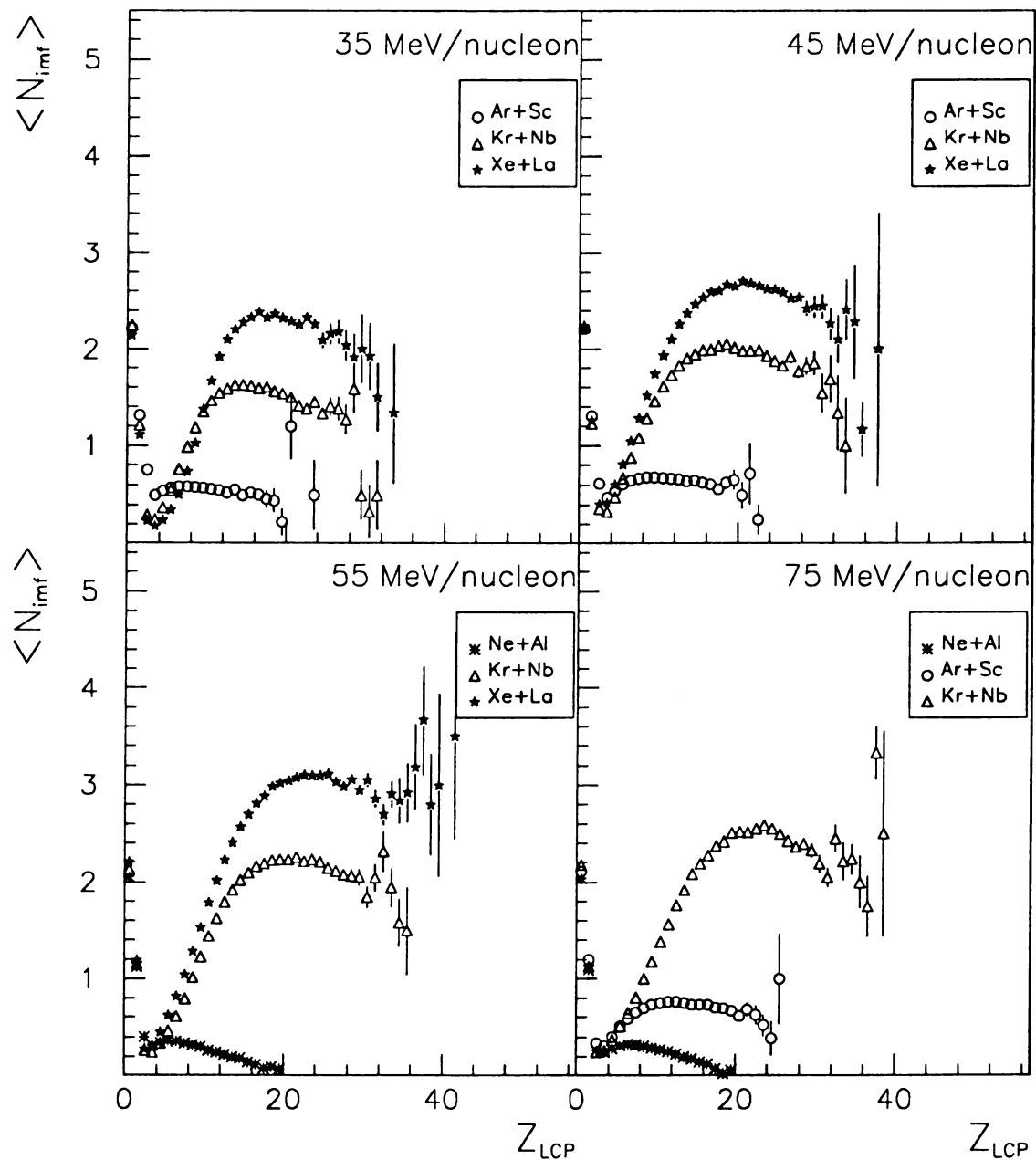


Figure 3.6: The entrance channel mass dependence of the average multiplicity of intermediate mass fragments versus the charge of the hydrogen and helium isotopes is plotted above. The symbols represent the systems available for the beam energies: 35 MeV/nucleon (upper left), 45 MeV/nucleon (upper right), 55 MeV/nucleon (lower left), and 75 MeV/nucleon (lower right). Corrections due to auto-correlations and experimental acceptance have not yet been made.

increasing beam energies.

The Ar+Sc system is the only one of the four in Figure 3.7 in which the curves representing $\langle N_{imf} \rangle$ for individual beam energies significantly cross at some point. This is an indication of a possible change in the reaction mechanism for increasing beam energies in nearly central collisions. Such transitions are characterized by maximal average multiplicities of IMF's.

Figure 3.8 depicts experimental $\langle N_{imf} \rangle$ values versus Z_{MR} for several beam energies in each of the four systems. In similarity to Figure 3.2, there is very little variation of the number of IMF's detected at specific values of Z_{MR} versus the beam energy in all systems.

The experimental values of the $\langle N_{imf} \rangle$ versus KE_T are plotted in Figure 3.9. In contrast to Figures 3.7 and 3.8, no significant beam energy dependence is seen for the Ne+Al system, but a significant dependence on the beam energy is seen in the three heavier systems, Ar+Sc, Kr+Nb, and Xe+La. The average number of IMF's in both the Kr+Nb and Xe+La systems increases monotonically with increasing beam energies. The opposite effect with respect to the beam energy was observed for the Ne+Al system in Figure 3.7.

The most significant variations between the four systems for specified beam energies occur in the plots of $\langle N_{imf} \rangle$ versus N_H and Z_{LCP} shown in Figures 3.10 and 3.11. These plots exhibit minima, maxima, and plateau regions. The curves representing each beam energy for the Ar+Sc system also cross, similar to that observed in earlier plots, indicating a possible transition. Overall, $\langle N_{imf} \rangle$ versus N_H and Z_{LCP} result in the lowest mean numbers of IMF's (see also Figures 3.5 and 3.6).

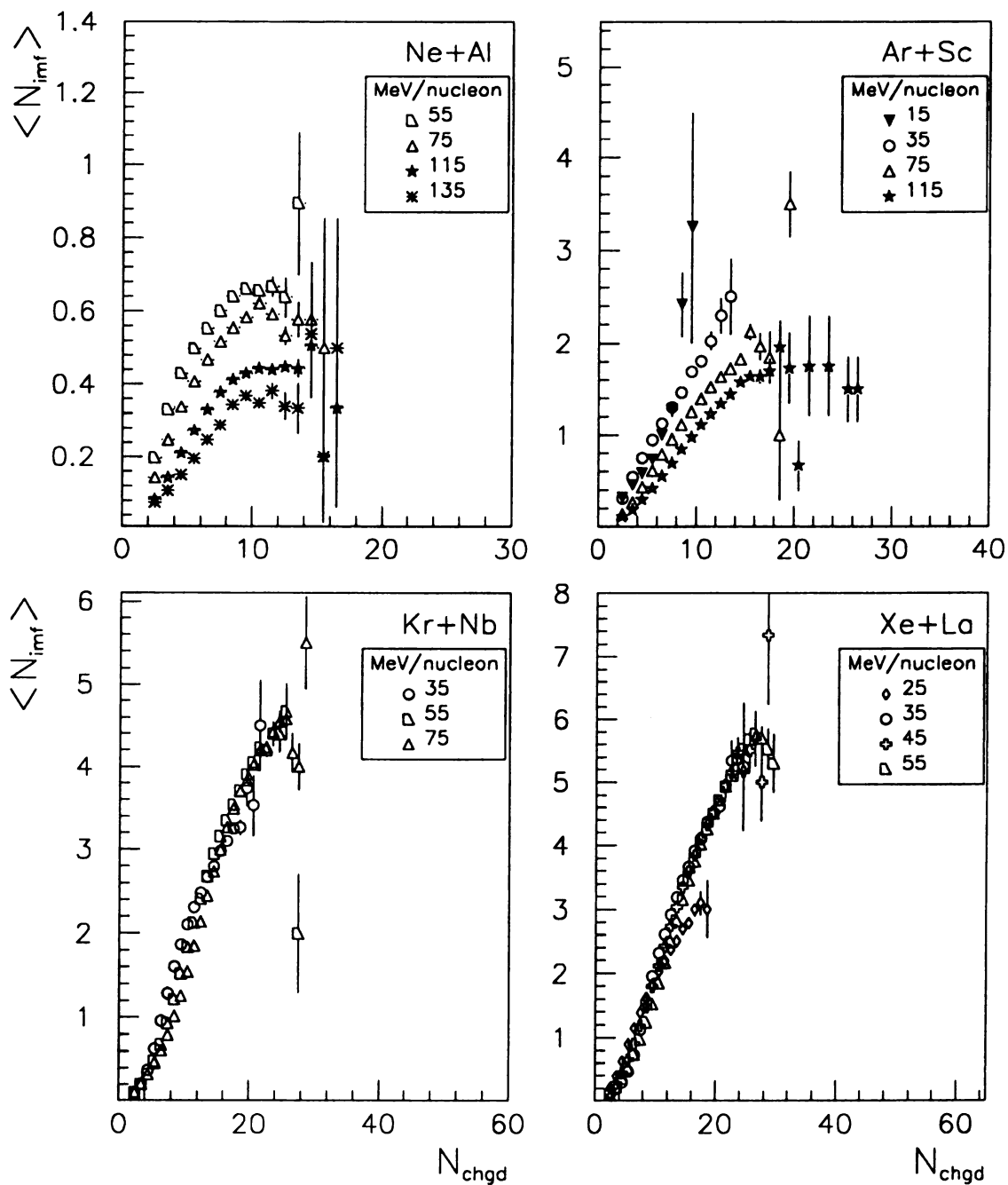


Figure 3.7: The beam energy dependence of the average multiplicity of intermediate mass fragments versus the number of charged particles for each of the four systems is plotted above, uncorrected. These systems are: $^{20}\text{Ne}+^{27}\text{Al}$ (top left), $^{40}\text{Ar}+^{45}\text{Sc}$ (top right), $^{84}\text{Kr}+^{93}\text{Nb}$ (bottom left), and $^{129}\text{Xe}+^{139}\text{La}$ (bottom right) for select beam energies in MeV/nucleon represented by the symbols indicated above.

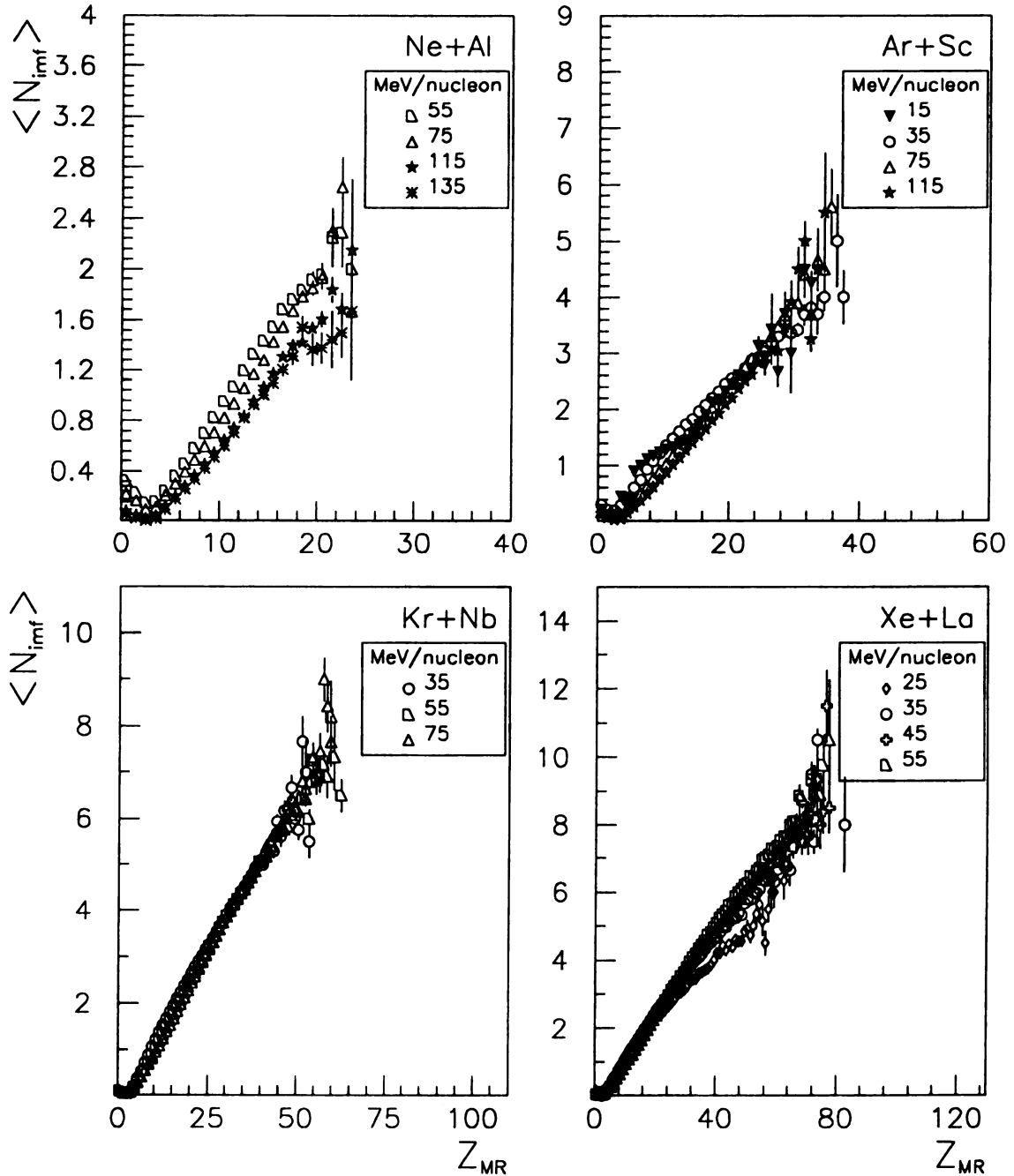


Figure 3.8: The beam energy dependence of the average multiplicity of intermediate mass fragments versus the charge detected at mid-rapidity for each of the four systems is plotted above. The select beam energies are represented by the symbols as: 15 MeV/nucleon (closed triangles), 35 MeV/nucleon (circles), 45 MeV/nucleon (open crosses), 55 MeV/nucleon (squares), 75 MeV/nucleon (open triangles), 115 MeV/nucleon (stars), and 135 MeV/nucleon (asterisks), for the four systems as indicated above. Correction have not yet been made for auto-correlations or experimental acceptance.

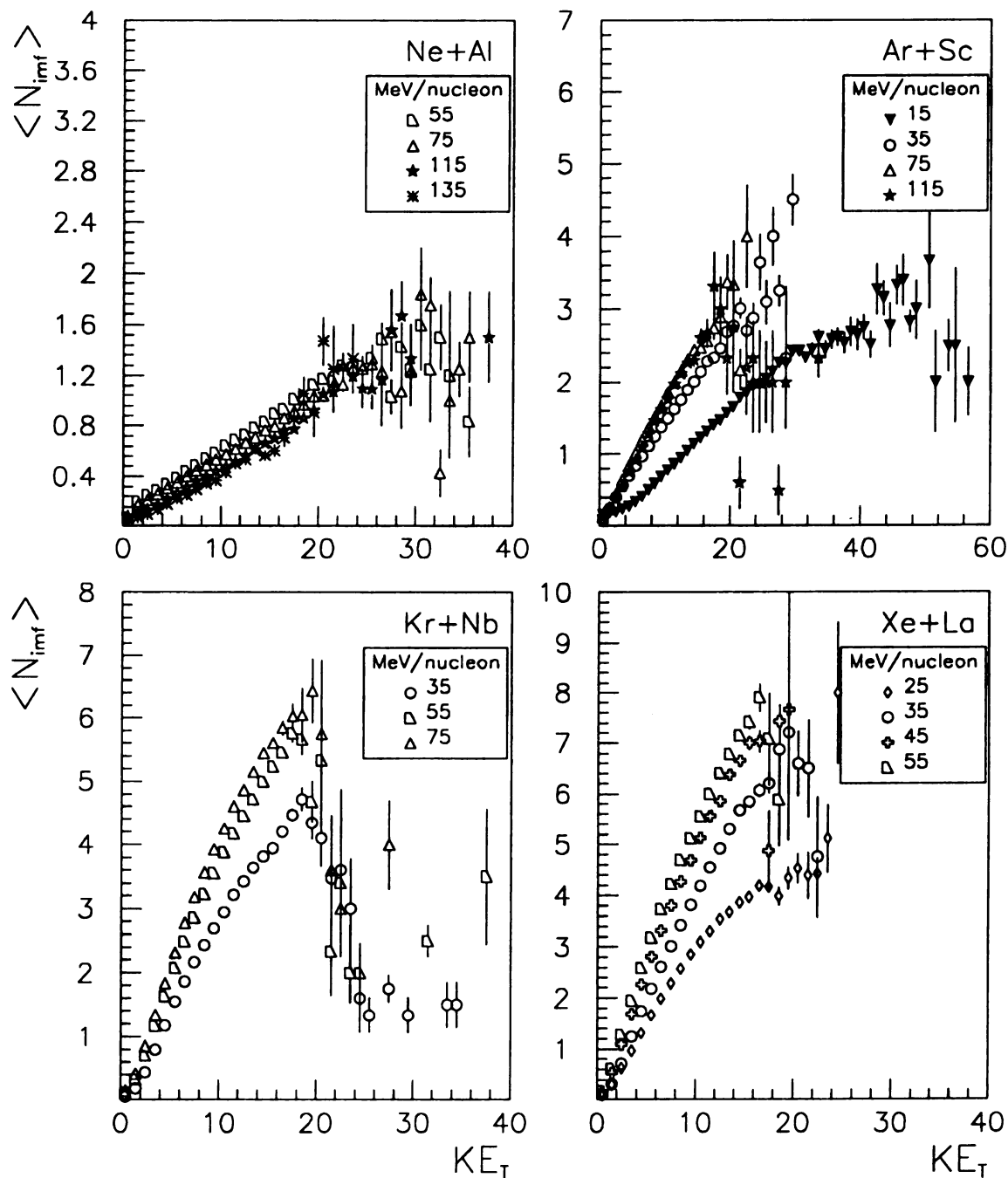


Figure 3.9: The beam energy dependence of the average multiplicity of intermediate mass fragments versus the total transverse kinetic energy for each of the four systems is plotted above, uncorrected. These systems are: $^{20}\text{Ne}+^{27}\text{Al}$ (top left), $^{40}\text{Ar}+^{45}\text{Sc}$ (top right), $^{84}\text{Kr}+^{93}\text{Nb}$ (bottom left), and $^{129}\text{Xe}+^{139}\text{La}$ (bottom right), for select beam energies in MeV/nucleon represented by the symbols indicated above.

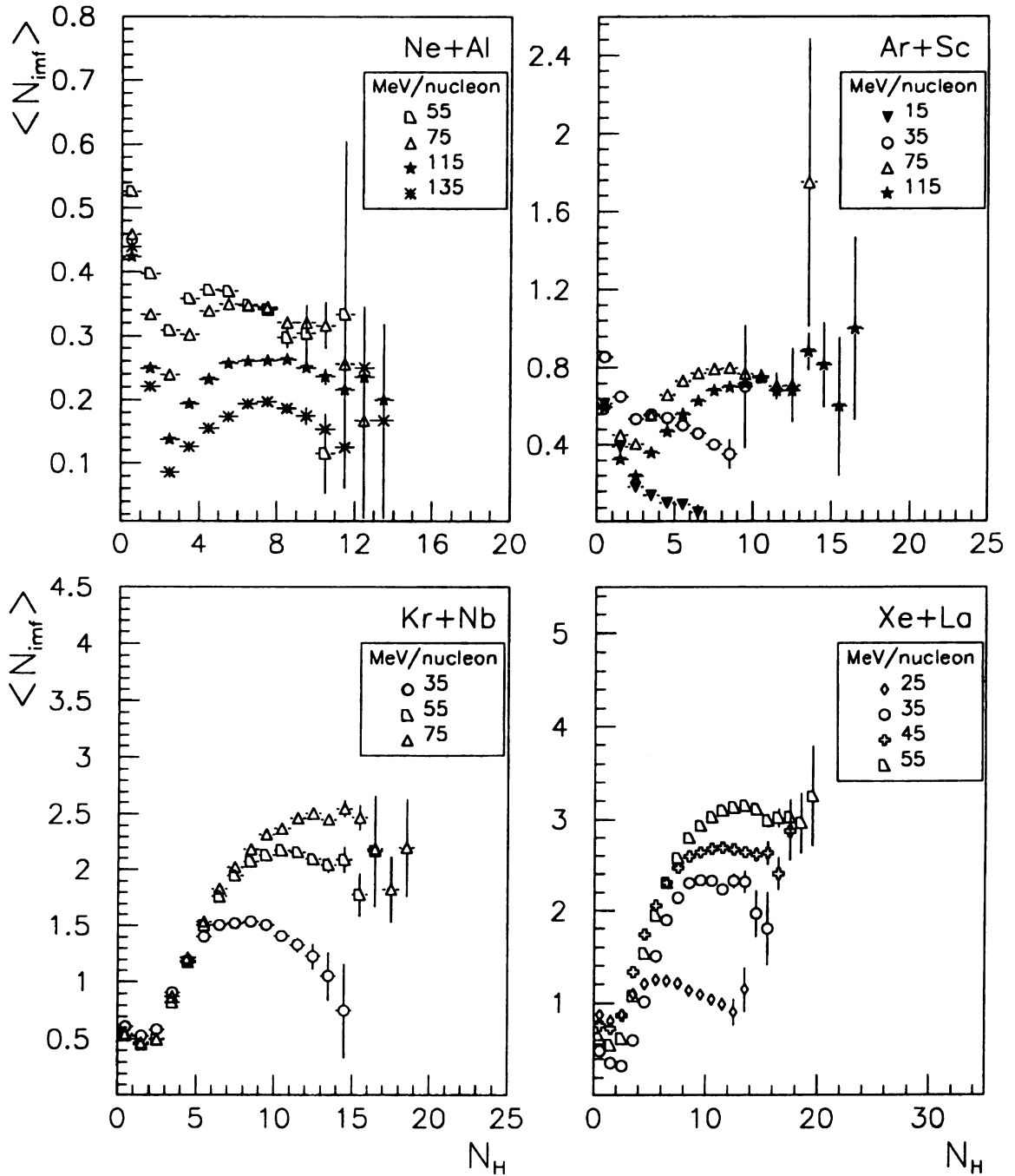


Figure 3.10: The beam energy dependence of the average multiplicity of intermediate mass fragments versus the number of hydrogen isotopes for each of the four systems is plotted above. The select beam energies are represented by the symbols as: 15 MeV/nucleon (closed triangles), 35 MeV/nucleon (circles), 45 MeV/nucleon (open crosses), 55 MeV/nucleon (squares), 75 MeV/nucleon (open triangles), 115 MeV/nucleon (stars), and 135 MeV/nucleon (asterisks), for the four systems as indicated above. Correction have not yet been made for auto-correlations or experimental acceptance.

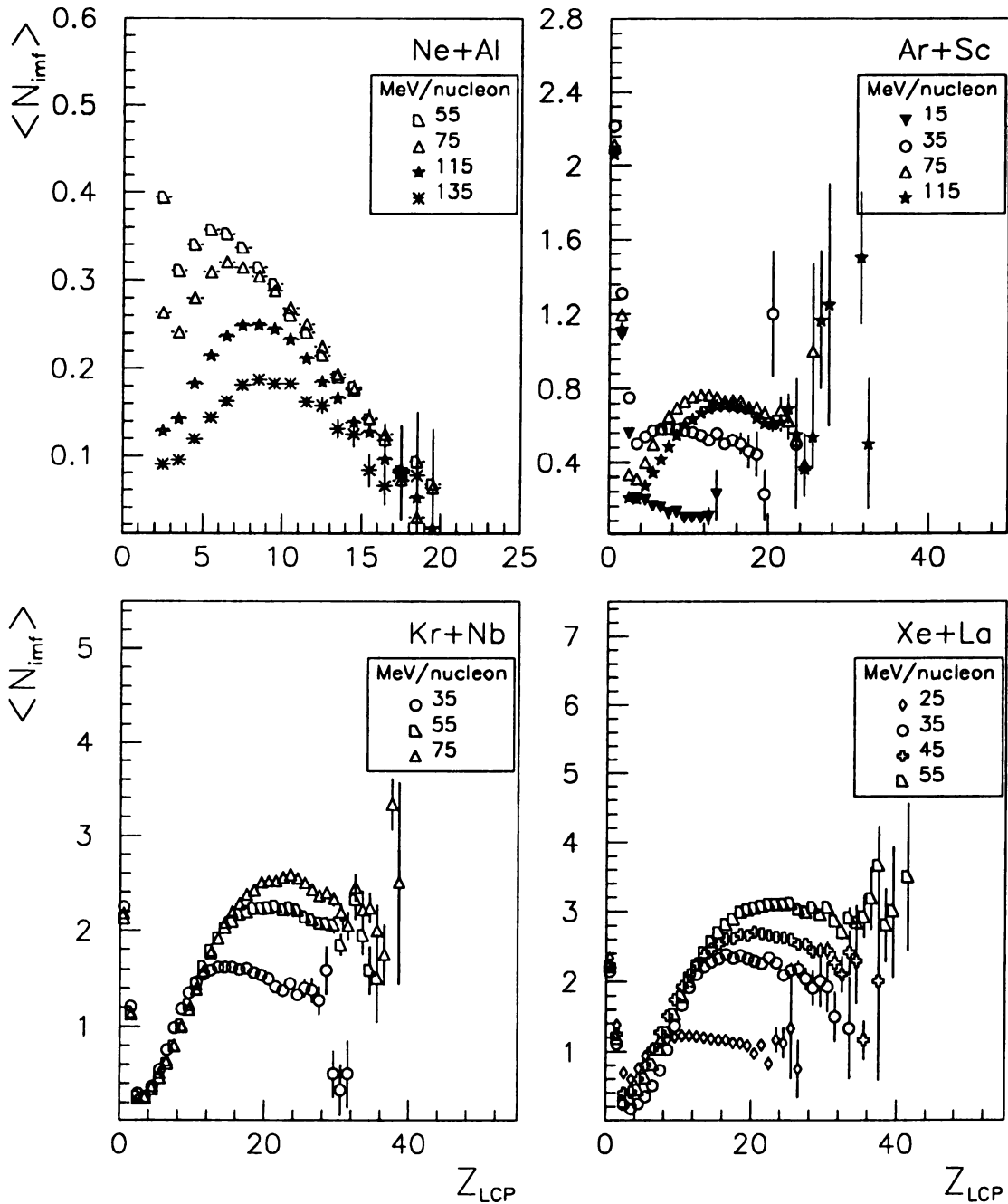


Figure 3.11: The beam energy dependance of the average multiplicity of intermediate mass fragments versus the charge of the hydrogen and helium isotopes for each of the four systems is plotted above, uncorrected. These systems are: $^{20}\text{Ne}+^{27}\text{Al}$ (top left), $^{40}\text{Ar}+^{45}\text{Sc}$ (top right), $^{84}\text{Kr}+^{93}\text{Nb}$ (bottom left), and $^{129}\text{Xe}+^{139}\text{La}$ (bottom right), for select beam energies in MeV/nucleon represented by the symbols as indicated above.

From the mass variation plots, Figures 3.1- 3.6, and the beam energy variation plots, Figures 3.7- 3.11, it can be concluded that cuts on the different centrality variables result in quantitatively different values of $\langle N_{imf} \rangle$. It is generally assumed that small values of these observables correspond to peripheral collisions, while the largest values correspond to the most central collisions.

There are wide fluctuations, however, in the observed average numbers of IMF's emitted and the general shape of the mean number of IMF curves when central collisions are selected using each of the various centrality variables. These variations in the IMF multiplicities suggest that the variables are not all as efficiently related to the impact parameter, or that auto-correlations exist between some of these centrality variables and $\langle N_{imf} \rangle$.

The selection of the top 10% of the spectra of any of the six centrality variables generally results in the most central events (i.e. those impact parameters (b) satisfying $\langle b \rangle / b_{max} \lesssim 0.22$) [1] [12]. More stringent cuts, such as the acceptance of a smaller percentage of events, are not expected to result in smaller selected impact parameters. The top 10% of each variable would then correspond to collisions resulting in the highest numbers of charged particles, the highest numbers of light charged particles, or the largest transverse kinetic energy of detected particles per event. These events might also exhibit the overall largest Z values registered in the detector or in a mid-rapidity gate. All of these conditions are consistent with those expected from the most violent of nuclear collisions. The central events are then only those that fall within the top $\sim 10\%$ of the N_{chgd} , Z_{MR} , KE_T , Z_{LCP} , and N_H values.

The mean number of IMF's of the events allowed by selecting the top 10% of the spectra of each of the centrality variables is plotted in Figure 3.12 as a function

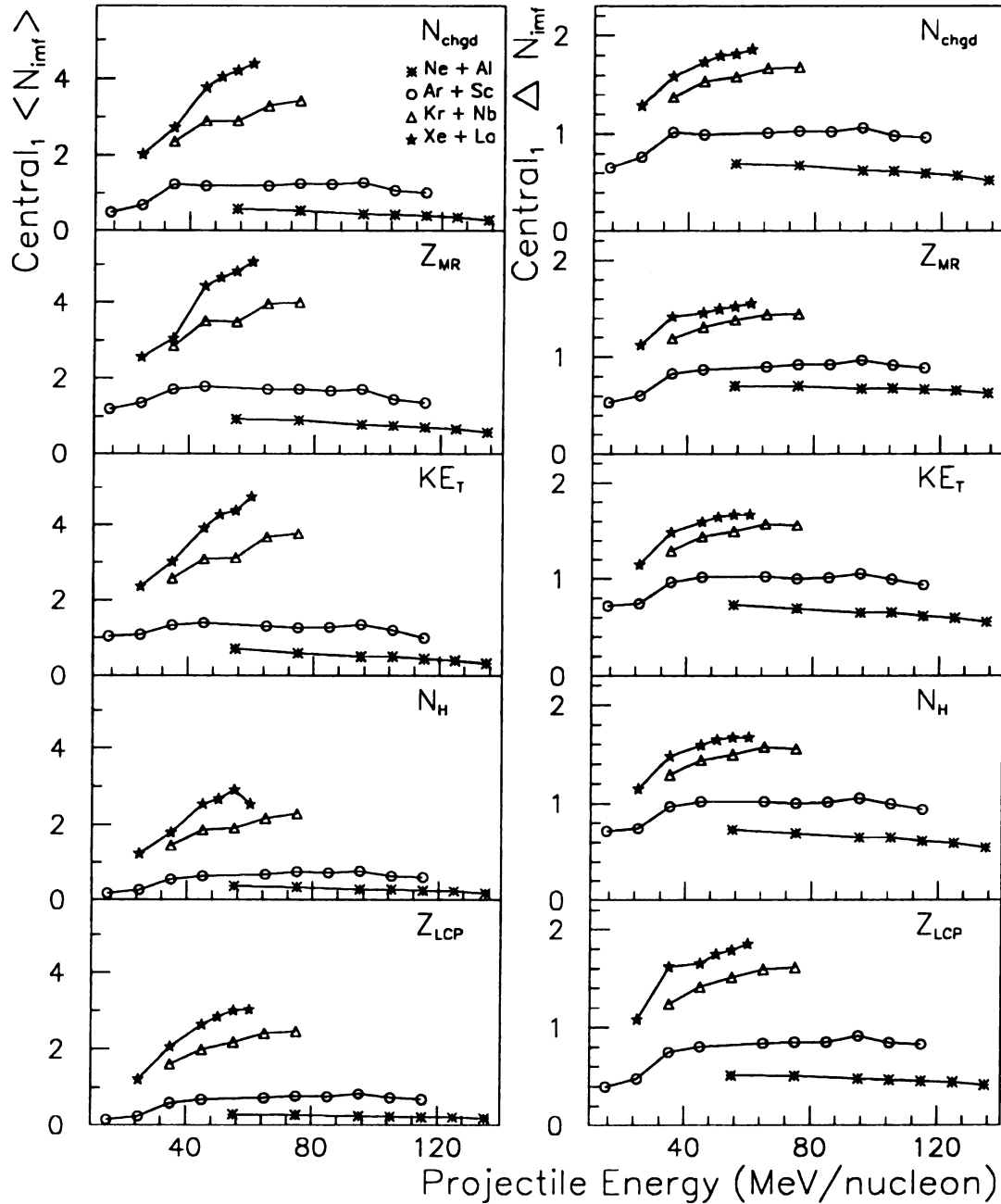


Figure 3.12: The beam energy dependence of the means and the widths of the intermediate mass fragment multiplicity distributions for the events selected by 10% cuts on each of the five centrality variables separately is plotted above. Central_1 denotes that this one dimensional cut was made. The left column contains the mean values uncorrected for experimental acceptance, and the right column contains the widths of the distributions for the four systems: $^{20}\text{Ne} + ^{27}\text{Al}$ (asterisks), $^{40}\text{Ar} + ^{45}\text{Sc}$ (circles), $^{84}\text{Kr} + ^{93}\text{Nb}$ (triangles), and $^{129}\text{Xe} + ^{139}\text{La}$ (stars).

of projectile kinetic energy for each of the four systems. The symbols represent the various entrance channels; Ne+Al by the asterisks, Ar+Sc by the circles, Kr+Nb by the triangles, and Xe+La by the stars. The left column of plots in Figure 3.12 is the experimental values of $\langle N_{imf} \rangle$ of events obtained through a cut on the top 10% of each centrality variable. This is denoted $Central_1$ to indicate a one dimensional cut is made on each centrality variable separately. The right column depicts the widths of the IMF distributions calculated via:

$$\Delta N_{imf} = \sqrt{\langle N_{imf}^2 \rangle - \langle N_{imf} \rangle^2}.$$

Figure 3.12 implies dramatic differences in the values of $\langle N_{imf} \rangle$ of fragments selected by the various cuts on the largest values of each centrality variable (as noted above). The Xe+La system consistently results in the highest mean values, and these numbers range from a maximum mean value of ~ 3 for cuts on N_H to a maximum mean value of ~ 5 for cuts on Z_{MR} .

The general trends in Figure 3.12 summarize the behavior of the right most values in each distribution in Figures 3.1- 3.11. These trends indicate that with increasing beam energy the experimental values of $\langle N_{imf} \rangle$ decrease for Ne+Al collisions, reach a slight maximum in Ar+Sc collisions near beam energies of 45 MeV/nucleon, and increase monotonically for the Kr+Nb and Xe+La systems. These distinctions can result from differences in the sensitivity of the various centrality variables to the impact parameter and from possible auto correlations between the centrality variables and the mean number of IMF's. To distinguish between these two possibilities, Section 3.2 will determine to what extent the mean values illustrated in Figure 3.12 are manifestations of such auto-correlations.

3.2 Auto-Correlations

The selection of the most central collisions on the basis of a cut on the largest values of a given centrality variable may, simply by definition, directly affect the values of the number of IMF's that are possible. This effect is a source of bias and needs to be removed from the analysis. If two variables are correlated, a plot of one variable versus the other would result in a distribution with a small width. If two variables were completely uncorrelated, then such a plot would result in a distribution with the largest possible width.

In this analysis, the multiplicity of the number of IMF's as a function of six separate centrality variables is used to determine a common unknown quantity - the impact parameter. Complications could result in utilizing these observables due to the fact that the variables could be auto-correlated with the number of IMF's detected. Cuts on such a variable could suppress or enhance the number of IMF's counted.

Two types of auto-correlations are possible: "positive" and "negative". Specific centrality cuts might artificially enhance the observed number of IMF's simply by definition. This type of artificial elevation will be denoted as a "positive auto-correlation". On the other hand, biases between the variables that result in artificially low values will be denoted as "negative auto-correlations." Both positive and negative auto-correlations between the centrality variable and the number of intermediate mass fragments are characterized by a relative suppression of the widths of the IMF distributions.

To avoid using the mean number of IMF's directly, the classification parameters for auto-correlation will be based on the variance of the IMF spectra ($\sigma_{N_{imf}}$) defined

as:

$$\sigma_{N_{imf}} = \langle N_{imf}^2 \rangle - \langle N_{imf} \rangle^2$$

and the variance normalized by the mean ($\sigma_{N_{imf}} / \langle N_{imf} \rangle$). Events from cuts on centrality variables resulting in a relatively small variance and a small normalized variance will be classified as “positive auto-correlators” since their effect is to artificially enhance the number of IMF’s that are observed. Conversely, events following cuts on centrality variables displaying a small variance of the number of IMF’s and a large normalized variance will be classified as “negative auto-correlators” since their effect is to automatically select collisions with small numbers of IMF’s.

To determine to what extent each centrality variable is correlated with N_{imf} , the means, widths, and reduced widths of the events selected through one dimensional $\sim 10\%$ cuts of the largest values of each centrality variable are plotted in Figures 3.13 and 3.14. The two lighter systems, Ne+Al and Ar+Sc, are shown in Figure 3.13, and the two heavier systems, Kr+Nb and Xe+La, are shown in Figure 3.14. In these Figures, the mean values are shown in the upper frames, the variances are shown in the middle frames, and the normalized variances are shown in the lower frames. All frames are plotted versus the available projectile kinetic energy for each system.

Auto-correlations are recognized by relatively small widths of the mean distributions. Furthermore, these auto-correlations between the variables can be classified as “positive” or “negative” auto-correlations with the number of IMF’s based on the normalized variances. Figures 3.13 and 3.14 thus indicate that three distinct groups form in all four systems appearing approximately always in the same order. Centrality cuts on the variables Z_{MR} and Z_{det} consistently display the largest mean values and the smallest reduced variances, N_H and Z_{LCP} consistently display the

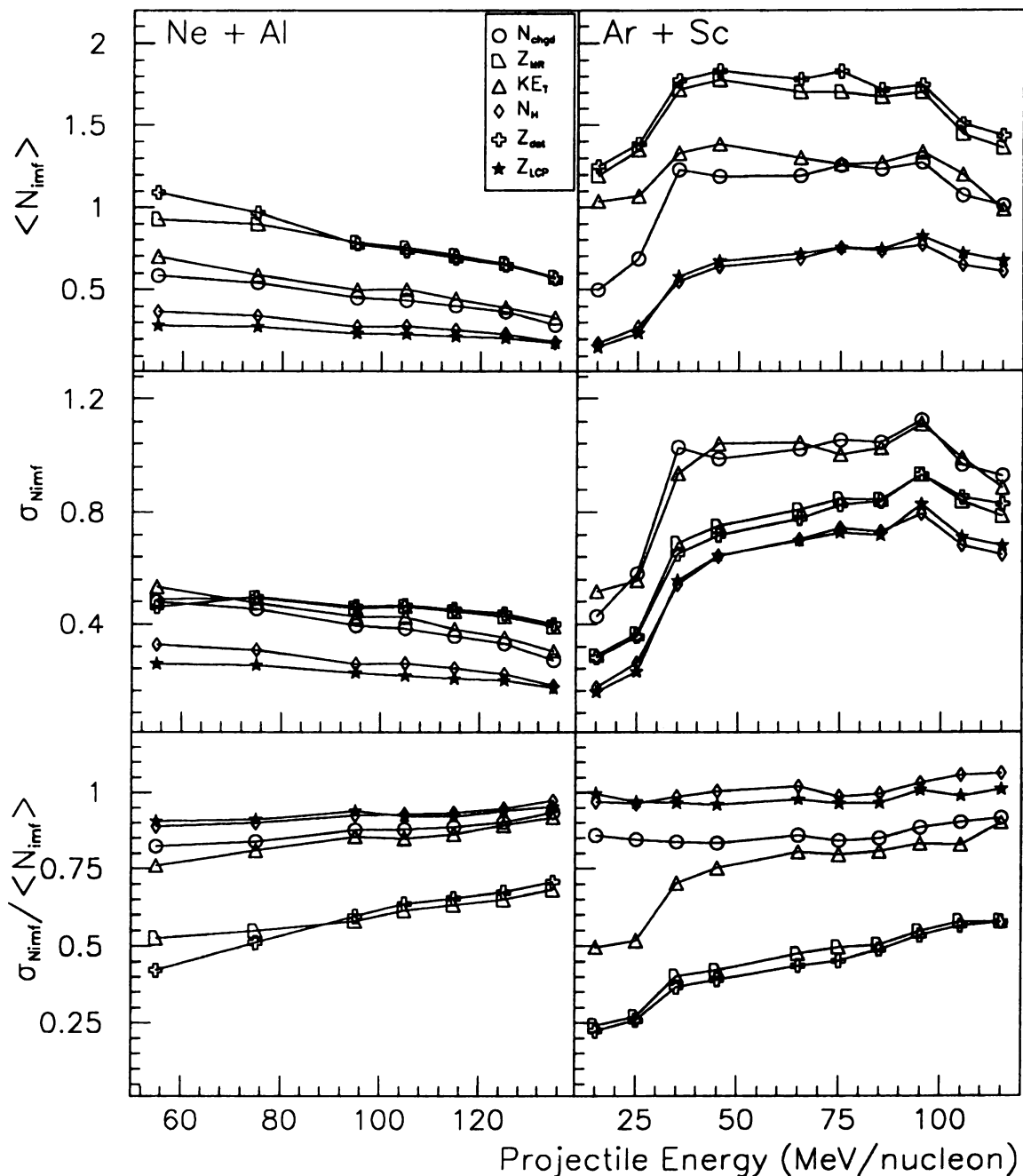
Central₁

Figure 3.13: The average values, widths, and reduced widths of the multiplicities of intermediate mass fragments in the events selected by $\sim 10\%$ cuts on the largest values of six centrality variables versus the beam energies for $^{20}\text{Ne} + ^{27}\text{Al}$ and $^{40}\text{Ar} + ^{45}\text{Sc}$ entrance channels are plotted above. Central₁ denotes that this one dimensional cut was made. The six centrality variables are labeled by symbols as indicated above. This data is not yet corrected for experimental inefficiencies.

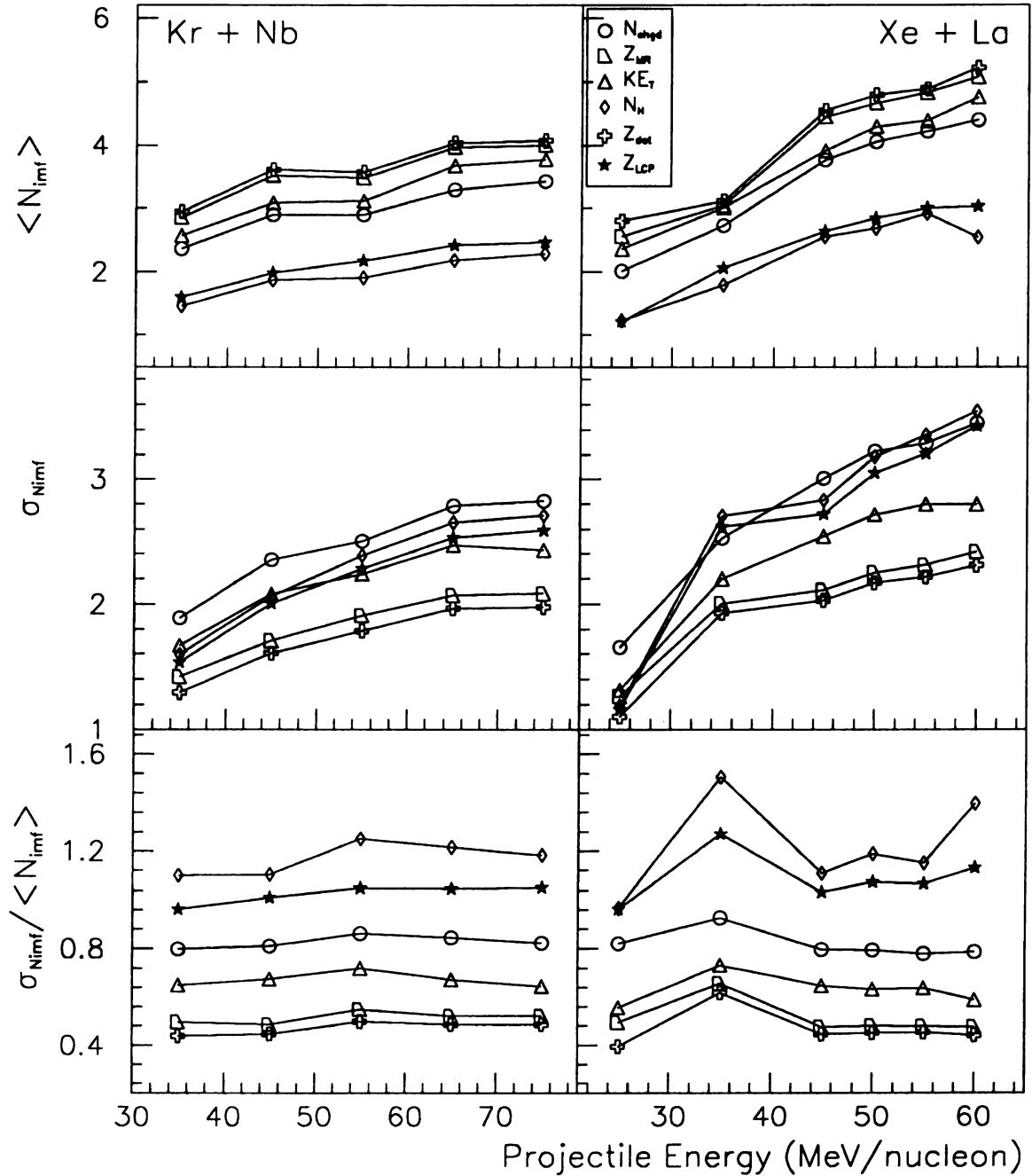
Central₁

Figure 3.14: The average values, widths, and reduced widths of the multiplicities of intermediate mass fragments in the events selected by $\sim 10\%$ cuts on the largest values of six centrality variables versus the beam energies for $^{84}\text{Kr}+^{93}\text{Nb}$ and $^{129}\text{Xe}+^{139}\text{La}$ entrance channels are plotted above. Central₁ denotes that this one dimensional cut was made. The six centrality variables are labeled by symbols as indicated above. This data is not yet corrected for experimental inefficiencies.

smallest mean values and the largest reduced variances, and N_{chgd} and KE_T consistently fall in the middle for both values. The middle frames, representing the variances, are not as structured due to the fact the three groups cross and even separate at some points. On average, the variables N_{chgd} and KE_T tend to have the larger widths or variances while Z_{MR} , Z_{det} , N_H , and Z_{LCP} tend to have the smaller variances.

The fact that these groups are clustered independent of energy indicates that they are the consequence of an internal effect rather than physical one. The conclusion is drawn that the formation of these groups reflects varying degrees of auto-correlations. The relative extent to which each variable is auto-correlated with the number of IMF's can then be determined from these plots.

Applying the guidelines defined above to Figures 3.13 and 3.14, Z_{MR} and Z_{det} have small widths as well as small reduced widths, hence they can be classified as positive auto-correlators. Conversely, N_H and Z_{LCP} have small widths and large reduced widths and therefore can be classified as negative auto-correlators. The remaining two variables, N_{chgd} and KE_T , have the largest possible widths and intermediate reduced widths, hence these observables are the least affected by auto-correlations. Therefore, only cuts on N_{chgd} and KE_T will select nearly central collisions that are unbiased by auto-correlations with the observable, the number of IMF's.

New significance can now be attributed to the mean number of IMF plots in Figures 3.1- 3.11. Special attention should be placed on the plots of $\langle N_{imf} \rangle$ versus N_H and Z_{LCP} ; Figures 3.5, 3.6, 3.10, and 3.11. Both N_H and Z_{LCP} were determined in this section to be negative auto-correlators. As a result, plateau regions are formed at low values of $\langle N_{imf} \rangle$ in these plots. This "negative" effect

can also be seen not only through the overall low mean values but also through the artificial maximums in $\langle N_{imf} \rangle$ curves. These multiplicity maximums are the result of the negative auto-correlations decreasing the true mean number of IMF's present for large values of N_H and Z_{LCP} .

Chapter 4

Most Central Collisions

The preceding section utilized experimental observables to select small impact parameter collisions. It was determined that the largest values of these observables generally corresponded to collisions with the largest numbers of IMF's. In order to select the smallest impact parameters, only events that fell in the top 10% of each of the six centrality variables were chosen. From the widths of these distributions, the extent to which each observable was auto-correlated with the mean number of IMF's was also determined.

To improve the efficiency of selecting the most central collisions, a stricter cut is now performed involving the selection of the top 10% of two different centrality variables simultaneously in an event. The use of a "two dimensional" cut at least recovers some of the losses in efficiency for impact parameters selection that are more evident for one dimensional cuts.

One possible combination of two centrality variables for this "two dimensional" cut are those shown in Table 3.1. These centrality variables are the ones that were determined to be the most efficient in selecting central collisions solely based on the sphericity study [1] which is free from auto-correlations of any type.

The results of “two dimensional” cuts on the centrality variables shown in Table 3.1 are shown in Figure 4.1. The solid line is $\langle N_{imf} \rangle$ of events satisfying the two dimensional cuts. The axis is labeled $Central_2$ to indicate that a “two dimensional” cut was made. The symbols represent the two conditions that were used to make the cut for each system and beam energy. These points are the same values shown in Figures 3.12- 3.14. In Figure 4.1, N_H cuts are represented by the diamonds, Z_{MR} (squares), KE_T (triangles), and Z_{LCP} (stars). The mean values of the number of IMF’s are plotted versus the beam energy for each system. The statical errors in these mean values are negligible and are not drawn. The four systems, Ne+Al, Ar+Sc, Kr+Nb, and Xe+La, are plotted separately.

Figure 4.1 indicates that the “two dimensional” $\langle N_{imf} \rangle$ curve falls between the chosen variables for the two lighter systems, but mostly above the one dimensional variables for the heavier systems. Assuming that the largest numbers of IMF’s are seen in the most central collisions (see Figures 3.1- 3.11), if these two dimensional cuts effectively selected smaller impact parameters, then one would expect a larger number of IMF’s to result from the two dimensional cut (solid lines) than from either of the individual one dimensional cuts (symbols). It is evident from this plot that this is not the case.

Using the results of the auto-correlation analysis conducted in Section 3.2, discrepancies between the the assumptions in the paragraph above and the curves shown in Figure 4.1 can be understood. Figure 4.1 reveals that these discrepancies are purely the result of positive and negative auto-correlations which become important if the number of IMF’s is the experimental observable, as in this case.

In both the Ne+Al and Ar+Sc systems, N_H and Z_{LCP} are used as one of the two variables for the “two dimensional” centrality cut throughout the energy ranges.

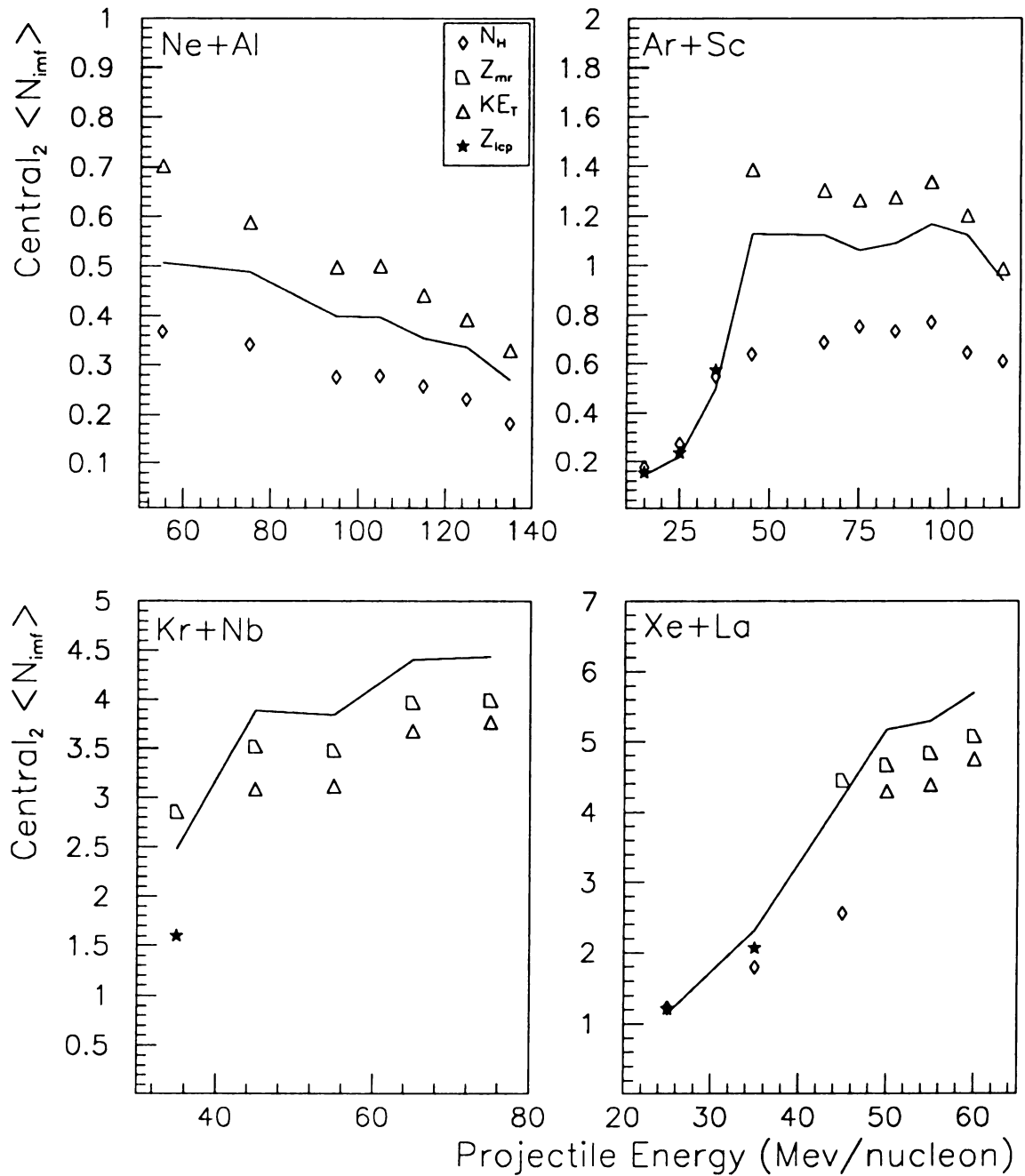


Figure 4.1: The mean number of intermediate mass fragments versus the beam energy for the events selected by the two most efficient centrality variables according to Reference [1] is plotted above. Central_2 denotes that this “two dimensional” cut was made. The symbols represent the results of the one dimensional cuts as indicated above. The solid line represents the more stringent cut hence the most central collisions for the four systems: $^{20}\text{Ne}+^{27}\text{Al}$ (upper left), $^{40}\text{Ar}+^{45}\text{Sc}$ (upper right), $^{84}\text{Kr}+^{93}\text{Nb}$ (lower left), and $^{129}\text{Xe}+^{139}\text{La}$ (lower right). This data is not corrected for the experimental acceptance of the detector.

These variables were seen to be negative auto-correlators and thus suppress the mean value of the number of IMF's. This is especially evident for beam energies of the Ar+Sc system that are less than 45 MeV/nucleon for which the variable Z_{LCP} was used. Conversely, the utilization of a positive auto-correlator, Z_{MR} , in the two variable centrality cut for the two heavier systems produces the opposite effect, artificially increasing the values of $\langle N_{imf} \rangle$ in the two dimensional cut.

It was determined in Section 3.2 that the variables N_{chgd} and KE_T are the two centrality variables that are least sensitive to auto-correlations with the average number of IMF's for the selected central collisions. These variables, however, are not the two most efficient variables in choosing central collisions [1]. Auto-correlations produce anomalous results and should be avoided, even at the risk of losing some sensitivity to the impact parameter. The only acceptable balance is then to maximize the efficiency of the selection of central collisions (i.e. from Reference [1]) while minimizing the contributions from auto-correlations during the specification of the variables upon which the cuts are made.

Taking both factors into consideration, a “two dimensional” cut is performed on the data set using the observables N_{chgd} and KE_T for all systems and beam energies. Only events falling in the top 10% of both variables are defined as the most central collisions.

Figure 4.2 depicts the average values of the multiplicity of IMF's in the events selected by this “two dimensional” cut on the centrality variables N_{chgd} and KE_T . This cut is also referred to as Central₂, but unlike the two dimensional cuts used to generate 4.1, these are free from auto-correlations for all systems and beam energies. The solid line represents the mean number of IMF's in the events accepted by the two dimensional N_{chgd} and KE_T cuts. The symbols represent the mean number of

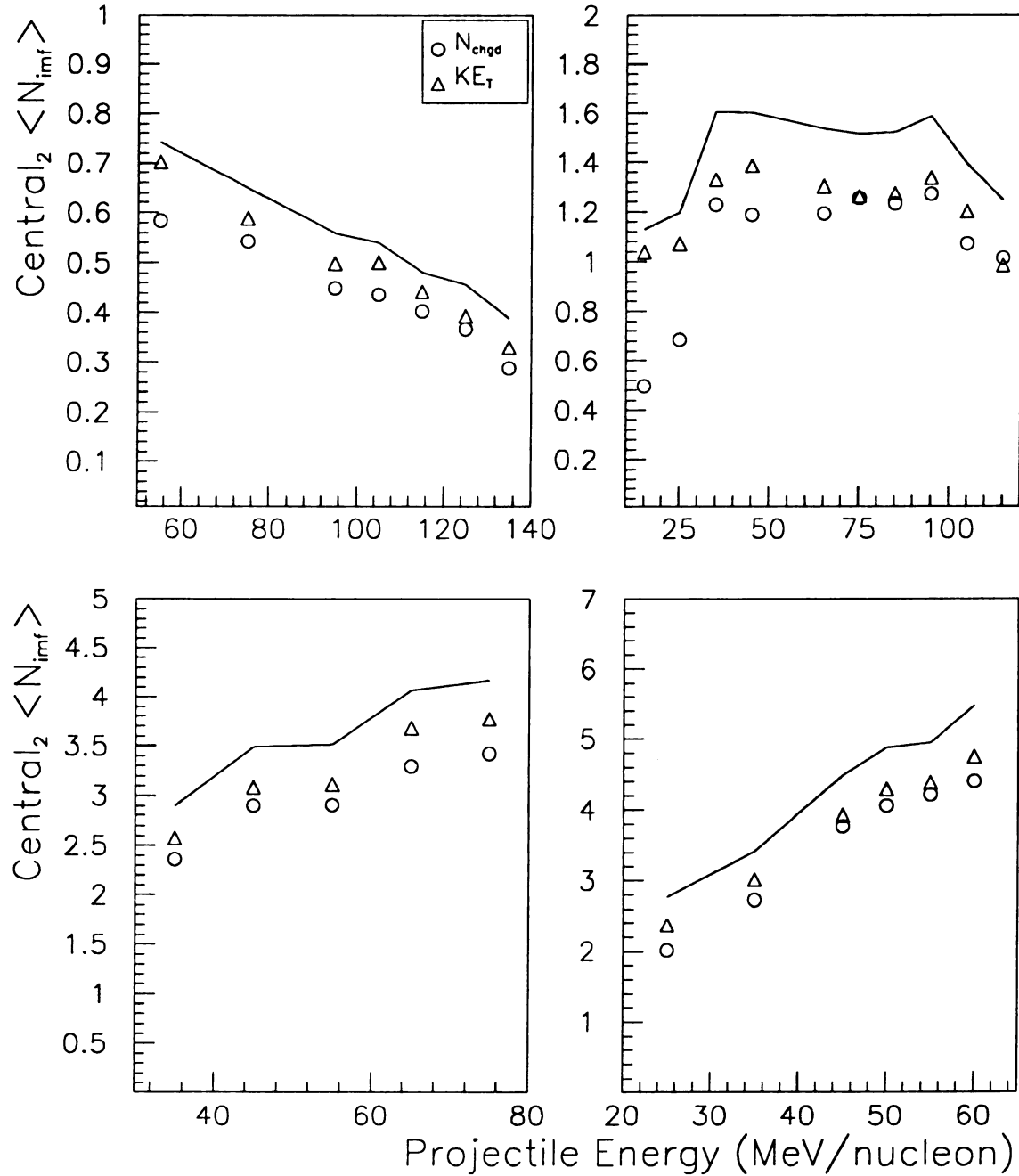


Figure 4.2: The mean number of intermediate mass fragments versus the beam energy for the events selected using the two centrality variables that were seen to be free from auto-correlations with the number of intermediate mass fragments and of relatively high efficiency according to Reference [1] is plotted above. Central_2 denotes that this “two dimensional” cut was made. The symbols are the one dimensional values with N_{chg} cuts represented by circles and KE_T cuts represented by triangles. The solid line represents the more stringent cut hence the most central collisions for the four systems: $^{20}\text{Ne}+^{27}\text{Al}$ (upper left), $^{40}\text{Ar}+^{45}\text{Sc}$ (upper right), $^{84}\text{Kr}+^{93}\text{Nb}$ (lower left), and $^{129}\text{Xe}+^{139}\text{La}$ (lower right). This data is not corrected for the experimental acceptance of the detector.

IMF's from each of the one dimensional cuts on N_{chgd} and KE_T separately that are used in determining the thresholds for the two dimensional slice. N_{chgd} cuts are represented by circles, and KE_T cuts are represented by triangles. As illustrated in the Figure, the selected events result in higher $\langle N_{imf} \rangle$ than either of the one dimensional cuts.

Figure 4.3 summarizes the above results by plotting these mean values obtained by the two dimensional cuts on the same axis for each of the four systems. The top plot is the experimental values of $\langle N_{imf} \rangle$ versus the projectile energy for the systems Ne+Al, Ar+Sc, Kr+Nb, and Xe+La as labelled. The bottom plot is the variances of the number of IMF distributions as defined previously. Figure 4.3 is then a representation of the experimental number of IMF's detected resulting from the best possible selection of central collisions that is free of auto-correlations but not yet corrected for experimental acceptance.

The probabilities for IMF emission are thought to be indicative of the phases of excited nuclear matter [3] [8], and changes in the average multiplicity of IMF's versus the beam energy is an indication of a transition region. By studying the IMF multiplicity in Figure 4.3, it can be inferred that the Ne+Al system is probably above this transition region, i.e. is in a gaseous stage, for the available projectile kinetic energies in this study (above 55 MeV/nucleon). The Kr+Nb and Xe+La systems, on the other hand, appear to be on the lower excitation energy side of such a transition for all the available beam energies. For these systems, increases in beam energy result in increases in the average numbers of IMF's in the most central collisions. Figure 4.3 apparently indicates a transition region in the Ar+Sc system occurring around a beam energy of ~ 45 MeV/nucleon. Such a maximum would be characteristic of a liquid-gas phase transition, if the assumption is valid that such

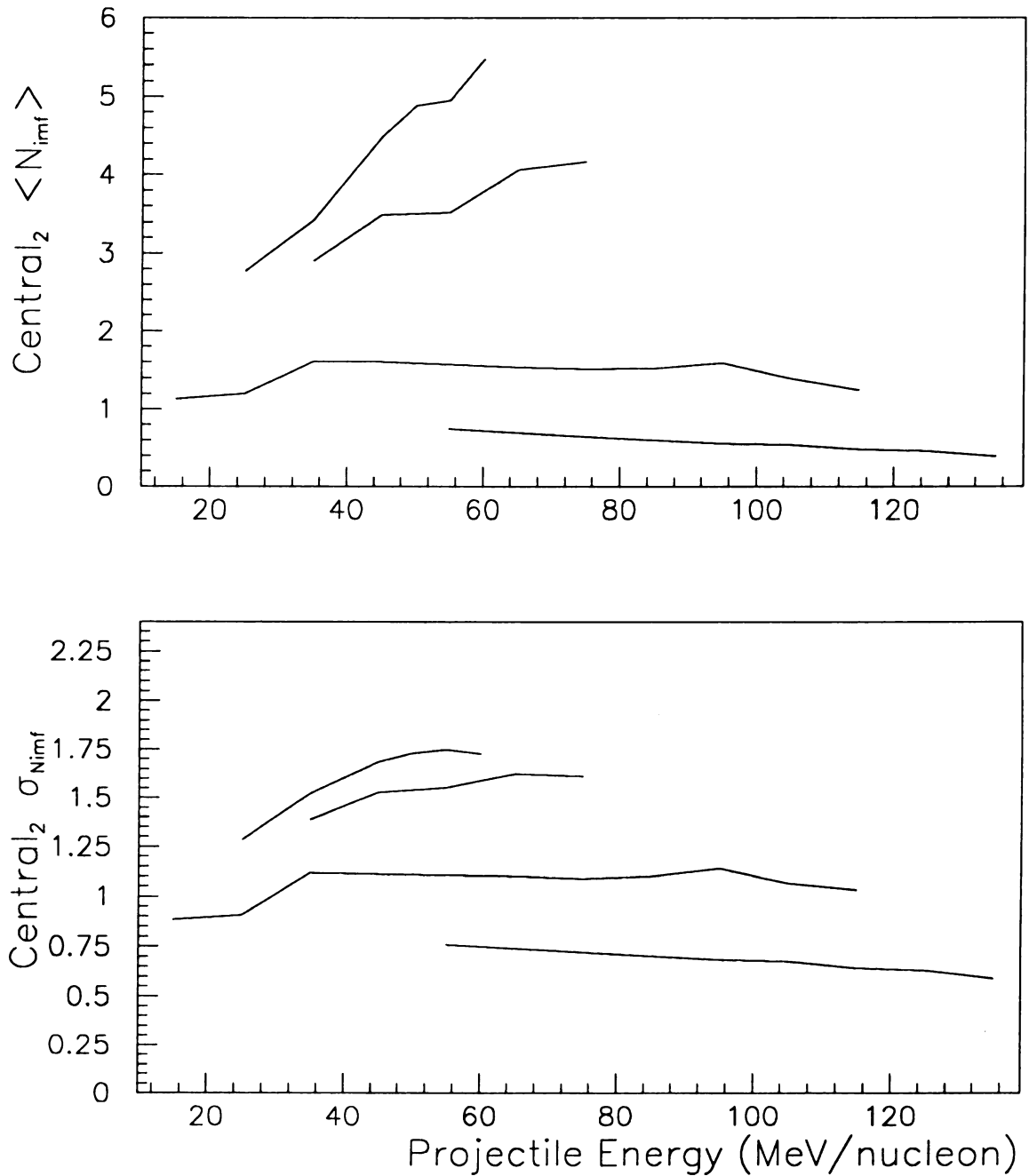


Figure 4.3: The mean number of intermediate mass fragments as a function of projectile energy for all of the systems is plotted above for the most central collisions. These are the mean values taken from Figure 4.2 and are not corrected for the acceptance of the detector. The bottom graph is the variance of the IMF distributions for the four systems: $^{20}\text{Ne}+^{27}\text{Al}$, $^{40}\text{Ar}+^{45}\text{Sc}$, $^{84}\text{Kr}+^{93}\text{Nb}$, and $^{129}\text{Xe}+^{139}\text{La}$.

a critical point maximizes that number of intermediate mass fragments. It should be noted that none of these curves have yet been corrected for the experimental acceptance dependence on the beam energy and the system mass.

Chapter 5

Discussion

In the preceding chapter, a cut was performed on the top 10% of two centrality variables in an effort to select the most central collisions. The variables N_{chgd} and KE_T were used for this selection process due to the fact that these variables are the least auto-correlated with the number of IMF's as well as reasonably efficient in selecting central collisions according to Reference [1]. From these “two dimensional” cuts, a representation of the number of intermediate mass fragments occurring in the most central collisions unbiased by auto-correlation was obtained. From the IMF multiplicity distributions, approximate regions of phase transitions in the decay mechanism of matter could be roughly identified as a function of beam energy although experimental corrections have not yet been performed. These results will now be compared with similar studies of IMF emission that have been previously reported.

The work of Li *et al.* [5] was conducted with the same $^{40}\text{Ar}+^{45}\text{Sc}$ system that was used in the present study. The centrality condition used in Reference [5] was an observable based on the number of charged particles, the total transverse momentum,

and the charge of the detected particles at mid-rapidity given by:

$$C = \left[\left(\frac{Z_{MR}}{Z_{tot}} \right) \left(\frac{P_{\perp}}{P_{proj}} \right) \left(\frac{N_{chgd}}{N_{max}} \right) \right]^{1/3},$$

where Z_{tot} is the total charge, N_{max} is the maximum number of particles, and P_{proj} is the total momentum of the projectile. Comparing the uncorrected data in Reference [5] to that shown in Figure 4.3, the mean number of IMF's are higher than that found in the present analysis (Figures 4.2 and 4.3) for the same system and beam energies. This is a result of the use of the variable Z_{MR} for the selection of central collisions in this previous work [5] which was found to be a positive auto-correlator (Section 3.2).

The research of Bowman *et al.* [3] was conducted with the Michigan State University Miniball which is a detector with similar acceptance to the one used in the present analysis. The work of Reference [3] involved a ^{129}Xe projectile beam at a kinetic energy of 50 MeV/nucleon impinging on the targets: ^{12}C , ^{27}Al , ^{51}V , ^{nat}Cu , ^{89}Y , and ^{197}Au . The mean numbers of IMF's as a function of the number of charged particles in this study can be compared to the present analysis (Figures 3.1 and 3.7). It is relevant to compare the mean number of IMF's reached in the largest values of N_{chgd} for each experiment which is shown in Figure 5.1. This plot is $\langle N_{imf} \rangle$ versus the entrance mass of the target for both studies. The results of Reference [3] are represented by the open circles, and the results of this analysis are represented by the asterisks. This plot illustrates that for masses below ~ 180 mass units, symmetric systems result in larger number of IMF's than the asymmetric systems. The reverse effect is true for systems larger than ~ 180 mass units; however, this difference could be purely the result of the slight differences in the acceptance of the two experiments.

It should be noted at this point that after auto-correlations are taken into consid-

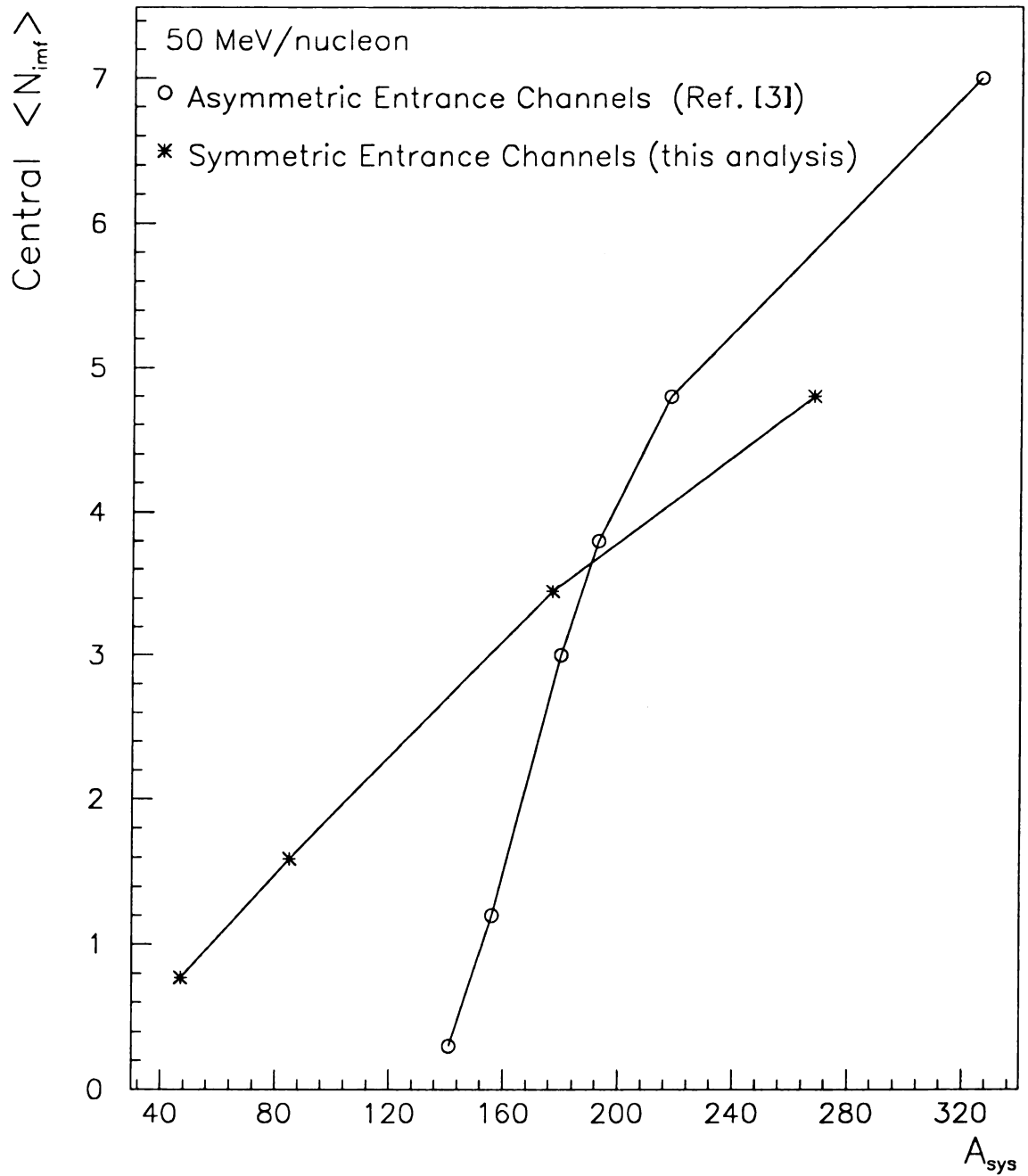


Figure 5.1: A qualitative comparison of the average number of intermediate mass fragments versus the entrance channel mass in symmetric (this work) versus asymmetric (Reference [3]) entrance channels is plotted above for a beam energy of 50 MeV/nucleon. The results from this analysis are represented by the asterisks and the results of Reference [3] are represented by the open circles.

eration, none of the plots of the mean values in Figures 3.1- 3.11 contain statistically significant maxima. The absence of maxima in these plots indicates that for the intermediate beam energies used in this study, the most central collisions contain the highest multiplicities of IMF's. At much higher beam energies, such as those studied by Ogilvie *et al.* [9], this was not the case. At these higher beam energies, the most numbers of IMF's were observed for intermediate impact parameters.

Further comparison with other work is limited due to the fact that results of the present analysis are not corrected for the acceptance of the detector. This sort of correction can be accomplished by generating events with model codes that reproduce the basic features of the data. Once a reasonable match is made, the efficiencies of the intermediate mass fragment measurements can be determined. Such studies are underway.

Chapter 6

Summary and Conclusions

The purpose of this analysis was to obtain a representation of the average number of intermediate mass fragments registered in a 4π geometry as a function of the kinetic energy of the projectile. Many different entrance channels: $^{20}\text{Ne}+^{27}\text{Al}$, $^{40}\text{Ar}+^{45}\text{Sc}$, $^{84}\text{Kr}+^{93}\text{Nb}$, and $^{129}\text{Xe}+^{139}\text{La}$, were utilized spanning a wide range of beam energies. Central collisions were of the most interest, and the centrality variables that were least correlated with the number of IMF's were identified.

To determine the extent of these auto-correlations, the mean number of intermediate mass fragments as well of the widths and the normalized widths of these distributions were plotted versus the beam energy. From these representations, it was determined that the number of charged particles in one event (N_{chgd}) and the transverse kinetic energy of emitted particles per event (KE_T) are the two centrality variables that are least correlated with the number of IMF's. Of the remaining four variables, the charge of detected particles at mid-rapidity (Z_{MR}) and the charge of all of the particles registered by the detector (Z_{det}), per event, were classified as positive auto-correlators. Conversely, the number of detected hydrogens (N_H) and the charge of the light charged particles (Z_{LCP}), per event, were classified as negative auto-correlators.

These results were then used to obtain a representation of the average number of IMF's observed for each central collision as a function of target mass and projectile energy that were unbiased by auto-correlations. Although the present results have not yet been acceptance corrected, there is a qualitative indicator that the $^{20}\text{Ne}+^{27}\text{Al}$ system results in a gaseous phase of nuclear matter for beam energies greater than 55 MeV/nucleon. The $^{84}\text{Kr}+^{93}\text{Nb}$ and $^{129}\text{Xe}+^{139}\text{La}$ systems appear to result in nuclear systems in a liquid phase for energies less than 75 MeV/nucleon, and the $^{40}\text{Ar}+^{45}\text{Sc}$ system appears to undergo a phase transition from liquid to gas around 40 - 70 MeV/nucleon. In the interest of quantifying these statements, future plans include the correction of the present measured average IMF multiplicities versus the beam energy for the inefficiencies of the experimental apparatus.

Bibliography

Bibliography

- [1] W.J. Llope, D. Craig, E. Gualtieri, S. Hannuschke, R.A. Lacey, T. Li, A. Nadasen, E. Norbeck, R. Pak, A. Vander Molen, G.D. Westfall, J.S. Winfield, J. Yee, and S.J. Yennello, *Phys. Rev. C*, submitted (1993).
- [2] G.D. Westfall, J.E. Yurkon, J. Van Der Plicht, Z.M. Koenig, B.V. Jacak, R. Fox, G.M. Crawley, M.R. Maier, B.E. Hasselquist, R.S. Tickle, and D. Horn, *Nucl. Inst. and Methods* **A238**, 347 (1985).
- [3] D.R. Bowman, C.M. Mader, G.F. Peaslee, W. Bauer, N. Carlin, R.T. de Souza, C.K. Gelbke, W.G. Gong, Y.D. Kim, M.A. Lisa, W.G. Lynch, L. Phair, M.B. Tsang, C. Williams, N. Colonna, K. Hanold, M.A. McMahan, G.J. Wozniak, L.G. Moretto, and W.A. Friedman, *Phys. Rev. C* **46**, 1834 (1992).
- [4] L. Phair, D.R. Bowman, C.K. Gelbke, W.G. Gong, Y.D. Kim, M.A. Lisa, W.G. Lynch, G.F. Peaslee, R.T. de Souza, M.B. Tsang, and F. Zhu, *Nucl. Phys.* **A548**, 489 (1992).
- [5] T. Li, W. Bauer, D. Craig, M. Cronqvist, E. Gualtieri, S. Hannuschke, R. Lacey, W.J. Llope, T. Reposeur, A.M. Vander Molen, G.D. Westfall, W.K. Wilson, J.S. Winfield, J. Yee, S.J. Yennello, A. Nadasen, R.S. Tickle, and E. Norbeck, *Phys. Rev. Lett.* **70**, 1924 (1993).
- [6] L. Phair, W. Bauer, D.R. Bowman, N. Carlin, R.T. de Souza, C.K. Gelbke, W.G. Gong, Y.D. Kim, M.A. Lisa, W.G. Lynch, G.F. Peaslee, M.B. Tsang, C. Williams, F. Zhu, N. Colonna, K. Hanold, M.A. McMahan, G.J. Wozniak, and L.G. Moretto, *Phys. Lett.* **B285**, 10 (1992).
- [7] G.D. Westfall, W. Bauer, D. Craig, M. Cronqvist, E. Gualtieri, S. Hannuschke, D. Klakow, T. Li, T. Reposeur, A.M. Vander Molen, W. K. Wilson, J.S. Winfield, J. Yee, S.J. Yennello, R. Lacey, A. Elmaani, J. Lauret, A. Nadasen, and E. Norbeck, *Phys. Rev. Lett.*, submitted (1993).
- [8] X. Campi, *Phys. Lett.* **B208**, 351 (1988).
- [9] C.A. Ogilvie, J.C. Adloff, M. Begemann-Blaich, P. Bouissou, J. Hubele, G. Imme, I. Iori, P. Kreutz, G.J. Kunde, S. Leray, V. Lindenstruth, Z. Liu, U. Lynen, R.J. Meijer, U. Milkau, W.F.J. Müller, C. Ngô, J.

- Pochodzalla, G. Raciti, G. Rudolf, H. Sann, A. Schüttauf, W. Seidel, L. Stuttge, W. Trautmann, and A. Tucholski, *Phys. Rev. Lett.* **67**, 1214 (1991).
- [10] D.R. Bowman, G.F. Peaslee, R.T. de Souza, N. Carlin, C.K. Gelbke, W.G. Gong, Y.D. Kim, M.A. Lisa, W.G. Lynch, L. Phair, M.B. Tsang, C. Williams, N. Colonna, K. Hanold, M.A. McMahan, G.J. Wozniak, L.G. Moretto, and W.A. Friedman, *Phys. Rev. Lett.* **67**, 1527 (1991).
- [11] R.T. de Souza, L. Phair, D.R. Bowman, N. Carlin, C.K. Gelbke, W.G. Gong, Y.D. Kim, M.A. Lisa, W.G. Lynch, G.F. Peaslee, M.B. Tsang, H.M. Xu, F. Zhu, and W.A. Friedman, *Phys. Lett.* **B268**, 6 (1991).
- [12] C. Cavata, M. Demoulins, J. Gosset, M.C. Lemaire, D.L'Hôte, J. Poitou, and O. Valette, *Phys. Rev. C* **42**, 1760 (1990).
- [13] K. Hagel, M. Gonin, R. Wada, J.B. Natowitz, B.H. Sa, Y. Lou, M. Gui, D. Utley, G. Nebbia, D. Fabris, G. Prete, J. Ruiz, D. Drain, B. Chambon, B. Cheynis, D. Guinet, X.C. Hu, A. Demeyer, C. Pastor, A. Giorni, A. Lleres, P. Stassi, J.B. Viano, and P. Gonthier, *Phys. Rev. Lett.* **68**, 2141 (1992).
- [14] W.A. Friedman, *Phys. Rev. C* **42**, 667 (1990).
- [15] G.F. Bertsch and P.J. Siemens, *Phys. Lett.* **B126**, 9 (1983).
- [16] L.G. Moretto, K. Tso, N. Colonna, and G.J. Wozniak, *Phys. Rev. Lett.* **69**, 1884 (1992).
- [17] W. Bauer, G.F. Bertsch, and H. Schulz, *Phys. Rev. Lett.* **69**, 1988 (1992).
- [18] D.H. Boal and J.N. Glosli, *Phys. Rev. C* **37**, 91 (1988).
- [19] Y.D. Kim, R.T. de Souza, D.R. Bowman, N. Carlin, C.K. Gelbke, W.G. Gong, W.G. Lynch, L. Phair, M.B. Tsang, F. Zhu, and S. Pratt, *Phys. Rev. Lett.* **67**, 14 (1991).
- [20] E. Baugu, A. Elmaani, R.A. Lacey, J. Lauret, N.N. Ajitanand, D. Craig, M. Cronqvist, E. Gualtieri, S. Hannuschke, T. Li, B. Llope, T. Reposeur, A. Vander Molen, G.D. Westfall, J.S. Winfield, J. Yee, S. Yennello, A. Nadasen, R.S. Tickle, and E. Norbeck, *Phys. Rev. Lett.* **70**, 3705 (1993).
- [21] D.A. Cebra, S. Howden, J. Karn, A. Nadasen, C.A. Ogilvie, A. Vander Molen, G.D. Westfall, W.K. Wilson, J.S. Winfield, and E. Norbeck, *Phys. Rev. Lett.* **64**, 2246 (1990).
W.A. Friedman and W.G. Lynch, *Phys. Rev. C* **70**, 16 (1983).
- [22] SA Ban-Hao and D.H.E. Gross, *Nucl. Phys.* **A437**, 643 (1985).
H.W. Barz, D.A. Cebra, H. Schulz, and G.D. Westfall, *Phys. Lett.* **B267**, 317 (1991).

MICHIGAN STATE UNIV. LIBRARIES



31293009049408